Annales Geophysicae (2003) 21: 509–538 © European Geosciences Union 2003

Annales Geophysicae

Ionospheric flow during extended intervals of northward but B_y-dominated IMF

A. Grocott[1], **S. W. H. Cowley**[1], **and J. B. Sigwarth**[2]

[1]Department of Physics and Astronomy, University of Leicester, Leicester LE1 7RH, UK
[2]Department of Physics and Astronomy, The University of Iowa, Iowa City, Iowa 52242-1479, USA

Received: 15 April 2002 – Revised: 3 July 2002 – Accepted: 20 August 2002

Abstract. We present SuperDARN radar observations of the nightside high-latitude ionospheric flow during two 6-hour intervals of quasi-steady northward interplanetary magnetic field (IMF). During both intervals (01:30–07:30 UT on 2 December and 21:00–03:00 UT on 14/15 December 1999), the solar wind and IMF remained relatively steady with B_z positive and B_y negative, such that the IMF clock angle was $\sim -50°$ to $-60°$. Throughout both intervals the radar data clearly indicate the presence of a highly distorted B_y-dominated twin cell flow pattern, indicative of an open magnetosphere, which is confirmed by DMSP and auroral data. Estimates of the changes in open flux present during each interval indicate approximately balanced dayside and nightside reconnection at rates of ∼30–35 kV over the full 6 h. However, strong bursts of flow with speeds of over $\sim 1000\,\mathrm{m\,s^{-1}}$ are observed near magnetic midnight on time scales of ∼1 h, which are associated with increases in the transpolar voltage. These are indicative of the net closure of open flux by reconnection in the tail. During one large flow burst, the nightside reconnection rate is estimated to have been ∼1.5 times the dayside rate, i.e. ∼45–60 kV compared with ∼30–40 kV. Magnetic bays, which would indicate the formation of a substorm current wedge, are not observed in association with these bursts. In addition, no low-latitude Pi2s or geostationary particle injections were observed, although some local, small amplitude Pi2-band (5–50 mHz) activity does accompany the bursts. Coincident measurements of the flow and of the low amplitude magnetic perturbations reveal nightside ionospheric conductances of no more than a few mho, indicative of little associated precipitation. Therefore, we suggest that the flow bursts are the ionospheric manifestation of bursty reconnection events occurring in the more distant geomagnetic tail. The main implication of these findings is that, under the circumstances examined here, the convection cycle is not equivalent to the usual substorm cycle that occurs for southward IMF.

Key words. Ionosphere (plasma convection; ionosphere-magnetosphere interactions) – Magnetospheric Physics (magnetotail)

Correspondence to: A. Grocott (ag27@ion.le.ac.uk)

1 Introduction

The dynamics of the Earth's coupled magnetosphere-ionosphere system is largely influenced by the orientation of the interplanetary magnetic field (IMF). More precisely, it depends primarily on the strength and orientation of the transverse GSM y and z components of the field, whose direction is given by the "clock angle", θ, with respect to north. Thus, a 0° clock angle corresponds to a transverse field purely in the $+z$ direction (northward), $\pm 90°$ to $\pm y$ (respectively), and $\pm 180°$ to $-z$ (southward). When the interplanetary field points south, i.e. when $|\theta| > 90°$, the dynamics of the system is dominated by Dungey-cycle flow and the substorm cycle (Dungey, 1961; Hones, 1979; Farrugia et al., 1993; Baker et al., 1996). Reconnection at the low-latitude magnetopause between the geomagnetic field and the IMF results in the formation of open flux tubes, which are transported anti-sunward by the solar wind and stored in the lobes of the geomagnetic tail. This process is dominant during the growth phase of substorms, and is associated with twin-vortex flow in the polar ionosphere, which is strongest on the dayside and is related to a concurrent expansion in the area of open flux in the polar cap (Siscoe and Huang, 1985; Cowley and Lockwood, 1992). Rapid excitation of polar convection during intervals of southward IMF is now a well-established phenomenon (e.g. Etemadi et al., 1988; Ruohoniemi et al., 1993; Ridley et al., 1998; Khan and Cowley, 1999), and even the sub-structure of individual magnetopause reconnection events ("flux transfer events") is well-resolved in dayside flow and auroral data (e.g. Lockwood et al., 1989; Elphic et al., 1990; Pinnock et al., 1993; Provan et al., 1998; Neudegg et al., 1999; Milan et al., 2000). Subsequently, reconnection of lobe flux tubes in the tail current sheet results in open flux closure and field line contraction back towards the Earth, thus completing the Dungey cycle.

It has long been supposed that the tail process dominates during the expansion and recovery phases of substorms. Recent results from the Geotail spacecraft indeed show that tail reconnection typically begins in the dusk sector plasma sheet at down-tail distances of ∼20–30 R_E within a few minutes of expansion phase onset signatures appearing on the ground,

and subsequently expands into the dusk and midnight sectors (Nagai et al., 1998; Petrukovich et al., 1998; Machida et al., 1999). This process should also excite twin-vortex flow in the polar ionosphere (additional to that driven simultaneously by magnetopause processes), but with the flow now being strongest on the nightside and related to a concurrent contraction in the area of the open flux in the polar cap. Evidence for flow excitation during substorm expansions has recently been presented by Opgenoorth and Pellinen (1998) and Grocott et al. (2002), though matters are generally complicated by additional flow suppression and polarisation effects associated with the strong conductivity gradients in the substorm-disturbed nightside ionosphere (e.g. Kirkwood et al., 1988; Morelli et al., 1995; Weimer, 1999; Gjerloev and Hoffman, 2001; Khan et al., 2001).

When the interplanetary field points north, it is well established that Dungey-cycle flow and substorm activity are reduced (e.g. Fairfield and Cahill, 1966; Reiff et al., 1981), though observations in the dayside ionosphere suggest that open flux tube production does not switch off entirely until the clock angle falls below $\sim$30°–40° (e.g. Sandholt et al., 1998a, b). At the same time, high-latitude reconnection between lobe field lines and the IMF begins, exciting additional flow cells, particularly on the dayside (e.g. Dungey, 1963; Russell, 1972; Reiff and Burch, 1985; Bristow et al., 1998; Sandholt et al., 1999, 2000, 2001). On the nightside under these conditions a variety of phenomena have recently been reported, whose physical connections have yet to be established. Huang et al. (2001) reported observations of quasi-sinusoidal nightside flow oscillations in SuperDARN radar data during an extended interval of modest northward IMF and small (typically $<$45°) clock angle. The flows had amplitudes $\sim$500 m s^{-1} and a period of $\sim$1 h, and were associated with the formation of large-scale clockwise flow vortices in the post-midnight sector which subsequently propagated toward dawn. The authors associate these flows with global oscillations of an essentially closed tail. Walker et al. (1998, 2002), on the other hand, have reported the occurrence of latitudinally-restricted ($\sim$1° north-south) bursts of high-speed ($\sim$2 km s^{-1}) westward flow in the pre-midnight sector under similar interplanetary conditions (weak IMF with small clock angle). These flow bursts had a $\sim$12 min recurrence time (four main cycles were observed), and appear to have occurred at the equatorward edge of the dusk convection cell. Walker et al. interpret the bursts as being due to sporadic energy release and field dipolarisation in the geomagnetic tail associated with a viscously-driven twin-vortex flow system. It was noted by Sutcliffe (1998) that Pi2 and weak (few tens of nT) midnight-sector bay activity occurred during these events.

In yet another apparent class of nightside phenomena, bursty flow events having larger spatial scales and longer time scales have been reported. De la Beaujardière et al. (1994) report the occurrence of bursts of equatorward-directed flow in nightside Sondrestrom radar data, which took place during a "quiet-time" interval in which the transverse components of the IMF were small and directed mainly northward. These flow bursts were initiated near the nightside open-closed field line boundary, had amplitudes up to several 100 m s^{-1}, and recur at $\sim$1 h intervals, lasting on each occasion for a few tens of minutes. Simultaneous auroral data show that each flow pulse was accompanied by an activation of the poleward-most arc system, in which a new east-west aligned arc formed poleward of the existing boundary, and subsequently moved equatorward, together with existing precipitation structures. This behaviour strongly suggests an origin in bursts of reconnection in the "quiet-time" tail. Poleward boundary auroral intensifications (PBIs) and arc "bifurcations" have subsequently been shown to occur commonly under a wide variety of conditions, both during "quiet" times, and in the growth, expansion and recovery phases of substorms (Lyons et al., 1999), often leading to the ejection of one or more north-south aligned auroral forms (called "auroral streamers") towards lower latitudes (Henderson et al., 1998). These longitudinally-restricted "streamers" have themselves been associated with the occurrence of narrow "bursty-bulk flow" (BBF) channels of earthward-directed flow in the plasma sheet (Baumjohann, 1990; Angelopoulos et al., 1992), Pi2-band (5–50 mHz) activity, and longitudinally-localised injections of energetic particles at geostationary orbit (Sergeev et al., 1999). The relationship between the "streamer" structures and the large-scale ionospheric flow has yet to be investigated in detail. However, Senior et al. (2002) have recently reported the occurrence of large-scale bursty flows in the "quiet time" nightside ionosphere during an interval of "intermediate" clock angles $>$45°. These flows have a recurrence time of $\sim$1 h, with substructure on tens of minutes time scales, similar to the bursts reported by de la Beaujardière et al. (1994), and take the form of surges of westward "return" flow in the dusk convection cell, several degrees wide in latitude, and extending in local time from post-midnight towards dusk.

From the above discussion it will be clear that the nightside ionosphere and geomagnetic tail for northward IMF is often anything but "quiet", and is instead characterized by a wealth of flow and precipitation phenomena having a variety of characteristics. However, the relationships between many of these phenomena have not yet been clarified, and no overall picture has yet emerged of the behaviour of the tail and conjugate ionosphere under these conditions. In this paper we aim to contribute to this issue through the study of SuperDARN radar observations of nightside flows and related parameters during two extended intervals in which the IMF clock angle remained relatively steady at intermediate values $\theta \sim -50°$ to $-60°$. Thus, IMF B_z was positive, but the largest transverse field component was IMF B_y, which was consistently negative. These intervals (on 2 and 14/15 December 1999) were sufficiently extended ($\sim$6 h each) that we may reasonably expect the magnetosphere to have reached a state entirely characteristic of those conditions, rather than, for example, being significantly influenced by prior intervals of differently-directed IMF. For these northward, but "intermediate" orientations of the IMF, we may thus expect on the basis of the above discussion that open flux production at

the magnetopause persisted at modest rates, and indeed we show below that IMF B_y-distorted twin-cell flow persisted throughout both intervals, with transpolar voltages typically in the range ∼20–40 kV. We might also anticipate the excitation of "lobe" convection cells on the dayside. However, because we have chosen to study intervals with good radar coverage of the nightside hours, coverage of the dayside flows is not extensive in these data. Thus, the presence or absence of lobes cells is not well determined by these data and does not form a major topic of discussion.

With regard to nightside phenomena, however, a significant question exists concerning the magnetospheric response to modest but steady dayside driving under these conditions. During the growth phase of substorms with the IMF directed southward, the transpolar voltage (and implied open flux input to the tail) is typically twice the above values (i.e. ∼60–80 kV), and generally ∼30–40 min elapses before reconnection and plasmoid formation is excited in the near-Earth tail at substorm expansion phase onset. We may then ask whether substorms occur with reduced frequency or with reduced amplitude under conditions of reduced but continuous driving. In fact, we show in this paper that no classic substorm features were observed at all during these long intervals. Instead, large-scale bursts of flow were observed in the nightside ionosphere, having recurrence time scales of ∼1 h and lasting a few tens of minutes. These properties suggest a connection with the flow phenomena previously described by de la Beaujardière et al. (1994) and Senior et al. (2002), and thus also, possibly, with BBF/PBIs. In this paper we examine these flow observations in some detail, and discuss the implications for the balance between open flux production at the magnetopause and closure in the tail during northward IMF intervals of intermediate clock angle.

2 Instrumentation

In this section we provide brief details of the instrumentation employed in this study, which concerns the intervals 01:30–07:30 UT on 2 December and 21:00–03:00 UT on 14/15 December 1999.

2.1 SuperDARN radar data

The measurements of ionospheric convection velocities provided by the Super Dual Auroral Radar Network (SuperDARN) represent the central focus of our study. SuperDARN is an international array of HF coherent radars spanning the auroral regions of both the Northern and Southern Hemispheres (Greenwald et al., 1995). At the time of the intervals described here, the Northern Hemisphere network (used primarily in this study) consisted of six radars, whose fields of view extended ∼12 h of magnetic local time (MLT). This is illustrated in Fig. 1a, which shows the fields of view of the six radars at the centre times of each of the two intervals, i.e. 04:30 UT on 2 December, and 00:00 UT on 14/15 December. With increasing magnetic local time, the fields of view in each map are of the Saskatoon (T), Kapuskasing (K), Goose Bay (G), Iceland West (W), Iceland East (E), and Finland (F) radars. These are shown on geomagnetic grids extending from the pole to 60° magnetic latitude, with noon at the top and dusk to the left. The coordinates are Altitude Adjusted Corrected Geomagnetic (AACGM) coordinates, a development of the PACE system discussed by Baker and Wing (1989). The fields of view of those radars from which line-of-sight data will be displayed below are shaded blue. These are the Saskatoon, Kapuskasing, Goose Bay, and Iceland West radars for the first interval, and the Goose Bay, Iceland West, Iceland East and Finland radars for the second. Data will be displayed from the beam directions marked by the red lines. It should be noted, however, that the fields of view of the radars changed significantly with respect to MLT over each interval, and encompassed the whole nightside ionosphere at ∼02:00 UT. Continuous observations of the whole nightside over an interval which extends on either side of this time are, therefore, not possible, a limitation which is reflected in the analysis of the flow data below. Data from the Southern Hemisphere network (which consisted of the four radars Tiger (R), Halley (H), Syowa (J), and Syowa East (N)) are also discussed below, although no detailed analysis is performed due to limited coverage. Their fields of view are, therefore, not shown here.

During both study intervals, all ten radars were operating in a standard mode in which each radar scans through 16 beams of azimuthal separation 3.24°, with a total scan time of 2 min. Each beam is divided into 75 range gates of length 45 km, and so in each full scan the radars cover 52° in azimuth and over 3000 km in range. Large-scale maps of the high-latitude convection have been derived from this data using the "Map Potential" model developed by Ruohoniemi and Baker (1998). The line-of-sight velocities are mapped onto a polar grid, and used to determine a solution for the electrostatic potential which is expressed in spherical harmonics. The equipotentials of the solution represent the plasma streamlines of the modelled convection pattern. Information from the statistical model of Ruohoniemi and Greenwald (1996), parameterised by concurrent IMF conditions, is used to stabilize the solution where no data are available. Here, spherical harmonic fits, which use terms up to sixth order, are employed to fit the Northern Hemisphere data, with the functions being expressed about a pole that has been shifted by 2° towards the nightside. A lower-latitude convection limit of 67° relative to this pole has also been imposed, as deemed appropriate for the contracted nature of the flow pattern during these two intervals (see Ruohoniemi and Baker (1998) for a detailed discussion of the Map Potential algorithm). The flow vectors which will be shown superposed on the electric equipotentials patterns are derived using the SuperDARN line-of-sight velocity measurements and the transverse velocity component from the spherical harmonic fit.

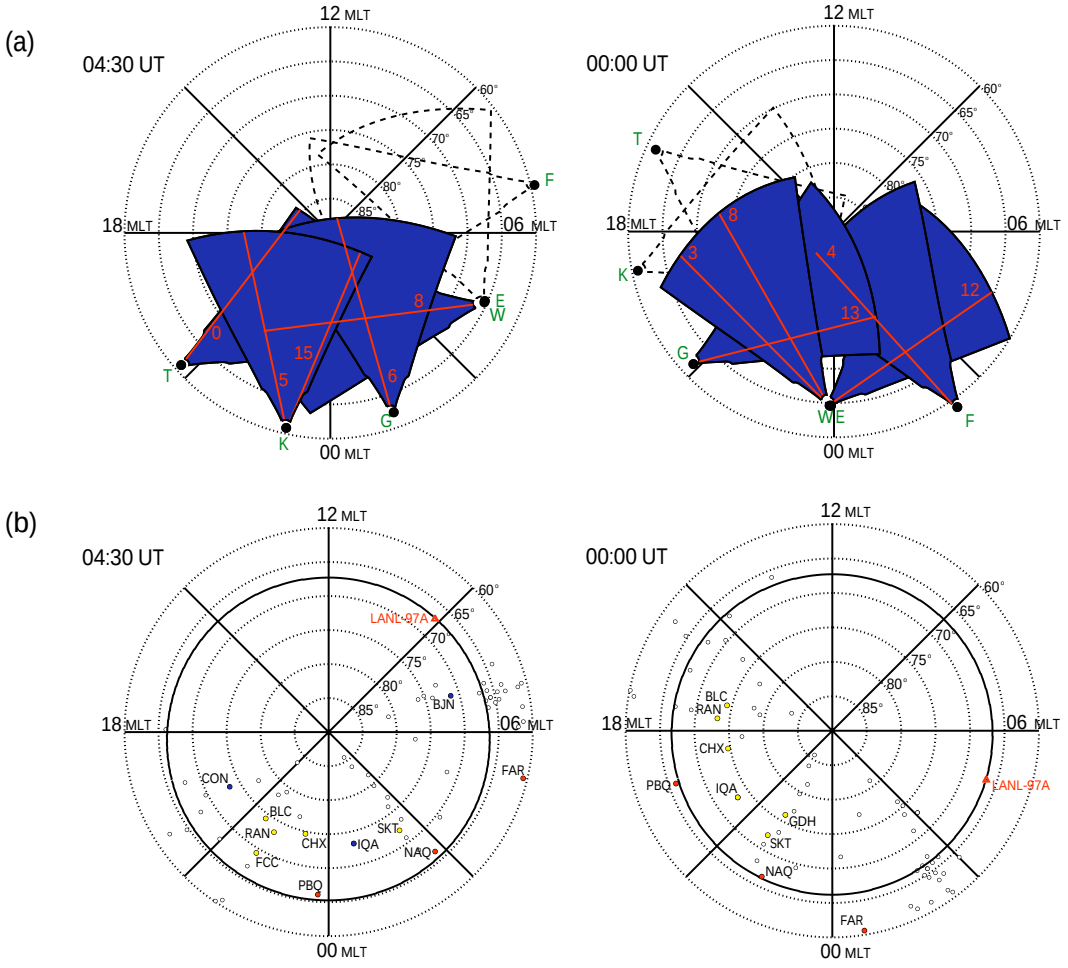

Fig. 1. (a) Fields of view of the six Northern Hemisphere SuperDARN radars at 04:30 (left) and 00:00 UT (right), the centre times of the two intervals considered in this paper. These are plotted on a geomagnetic grid from the pole to 60°, with 12 MLT at the top and dusk to the left. Fields of view coloured blue are those of the four radars for which detailed line-of-sight measurements will be discussed, using the beams indicated in red. **(b)** Shows ground-based magnetometer locations and the LANL spacecraft footprint at the same times on the same grid. Red dots indicate stations whose data has been band-pass filtered to provide information on Pi2 signals. Blue dots indicate three stations which span the local time extent of the radar fields of view. Yellow dots indicate stations which span individual events which are studied in detail. The black oval represents the ionospheric footprint of geostationary orbit.

2.2 Ground magnetometer data

Figure 1b shows the locations of the ground magnetic stations employed, indicated in the figure by the black circles on the same magnetic grids and at the same times as in Fig. 1a. Data have been inspected from all the magnetograms of six Northern Hemisphere arrays which span the same 12 h of MLT as the SuperDARN radars. These are the Canadian CANOPUS array (Grant et al., 1992), the Geological Survey of Canada array, the MACCS array (Hughes and Engebretson, 1997), the Greenland magnetometer chain (Friis-Christensen et al., 1985), the Scandinavian IMAGE array (Lühr et al., 1998), and the SAMNET array (Yeoman et al., 1990). Data from selected stations will be presented in H, D, Z coordinates, where H is local magnetic north, D is local magnetic east, and Z is vertically down. These stations are indicated in Fig. 1b by the coloured circles, and their identifier codes are also shown for reference. Data from those at lower latitudes and colour-coded red (i.e. PBQ, NAQ, and FAR) have been band-pass filtered (20–200 s), to provide information on substorm-related Pi2 signals. Those at latitudes ∼70°–75° and colour-coded blue (i.e. CON, IQA, and BJN) are distributed in longitude over the local time extent of the radar array, to give an indication of the overall magnetic activity during each interval. We will also show data from a number of sub-arrays, colour-coded yellow, which span individual features at much higher spatial resolution, thus enabling a more detailed analysis.

2.3 LANL geostationary spacecraft data

The occurrence of energetic ion and electron injections at geostationary orbit has been examined using data from the SOPA instruments carried by Los Alamos National Labo-

ratory (LANL) spacecraft (Belian et al., 1992). Data from three operating spacecraft, 1994-084, 1989-046, and LANL-97A have been examined. During both intervals, LANL-97A was located in the post-midnight sector, as appropriate for monitoring electron injections. This data is, therefore, presented here, being representative of the entire data set. The red coloured triangle on each map in Fig. 1b shows the ionospheric footprint of LANL-97A, mapped from geostationary orbit using the T-89 model (Tsyganenko, 1989). The black solid line shows the footprint of a complete orbit.

2.4 Polar auroral images

Images of the aurora were provided by the VIS instrument on the Polar spacecraft (Frank et al., 1995) during the interval on 2 December. This instrument viewed the whole of the northern polar ionosphere from the beginning of the interval at 01:30 UT up to ~03:00 UT, and provided images approximately every 5 min. These consist of 32.5 s integrations of UV photons at a wavelength of 130.4 nm. No images were available for the interval on 14/15 December.

2.5 DMSP auroral particle data

Measurements of ion and electron fluxes by the SSJ/4 instrument on board the DMSP F12, F13, and F14 spacecraft (Hardy et al., 1984) have been employed to examine the patterns of polar particle precipitation and their relationship to the plasma flow. The instrument points toward zenith at all times, and provides 1 s resolution spectra of ion and electron fluxes between 30 eV and 30 keV.

2.6 Upstream interplanetary parameters

Interplanetary conditions during each interval were monitored by the ACE spacecraft (Stone et al., 1998), located at GSM coordinates $(X, Y, Z) = (222, 21, -25)\,R_E$ during the 2 December interval and $(X, Y, Z) = (226, 36, -15)\,R_E$ during the 14/15 December interval. The variation of the spacecraft position over each interval was not significant. Solar wind and IMF data were obtained by the SWEPAM and MAG instruments, respectively (McComas et al., 1998; Smith et al., 1999). The propagation delay of field changes from ACE to the dayside ionosphere has been estimated using the algorithm of Khan and Cowley (1999). This estimate includes the propagation time in the solar wind upstream of the bow shock, the frozen-in transit time across the subsolar magnetosheath, and the Alfvénic propagation time along open field lines from the subsolar magnetopause to the cusp ionosphere. With solar wind proton number densities n_p ~15 cm^{-3} and speeds v_p ~330 km s^{-1}, we find a propagation delay of 76±3 min for the 2 December interval. For 14/15 December, n_p was ~5 cm^{-3} and v_p ~380 km s^{-1}, giving a propagation delay of 68±5 min. These times have been used to lag the ACE solar wind and IMF data displayed here. It should be noted that during the 2 December interval, no data were available from ACE/SWEPAM from ~03:30 to ~06:30 UT. Therefore, we have used data from the Geotail CPI instrument (Frank et al., 1994) to give an indication of n_p and v_p during this period. A negligible propagation delay existed between Geotail and the ionosphere, due to Geotail's location at $(X, Y, Z) \approx (15, -20, 2)\,R_E$, consistent with features observed in both the ACE and Geotail data sets from before and after the ACE/SWEPAM data dropout.

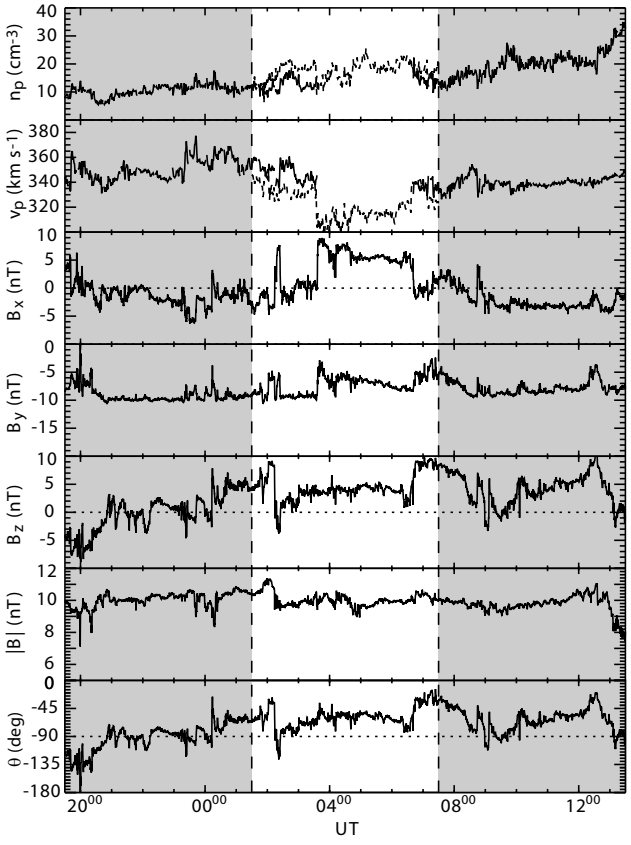

Fig. 2. Upstream interplanetary observations from the ACE spacecraft for 19:30 UT on 1 Dec to 13:30 UT on 2 Dec 1999, lagged by 76 min to account for the propagation delay to the ionosphere. The top two panels show solar wind density and velocity data (the dashed line represents data from Geotail, which was used where data was missing from ACE). The middle three panels show IMF data in GSM coordinates, and the bottom two panels show the field magnitude and clock angle. The clock angle is defined with respect to north, such that 0° corresponds to a transverse field purely in the $+z$ direction (northward), ±90° to $\pm y$ (respectively) and ±180° to $-z$ (southward).

3 Observations overview: Interval 1 (01:30–07:30 UT 2 December 1999)

In this section we discuss the ground and space observations made during the first of the two 6-hour intervals examined here, on 2 December 1999. We begin with an overview of the interplanetary data, and subsequently look in more detail at the magnetic, flow, particle, and auroral data.

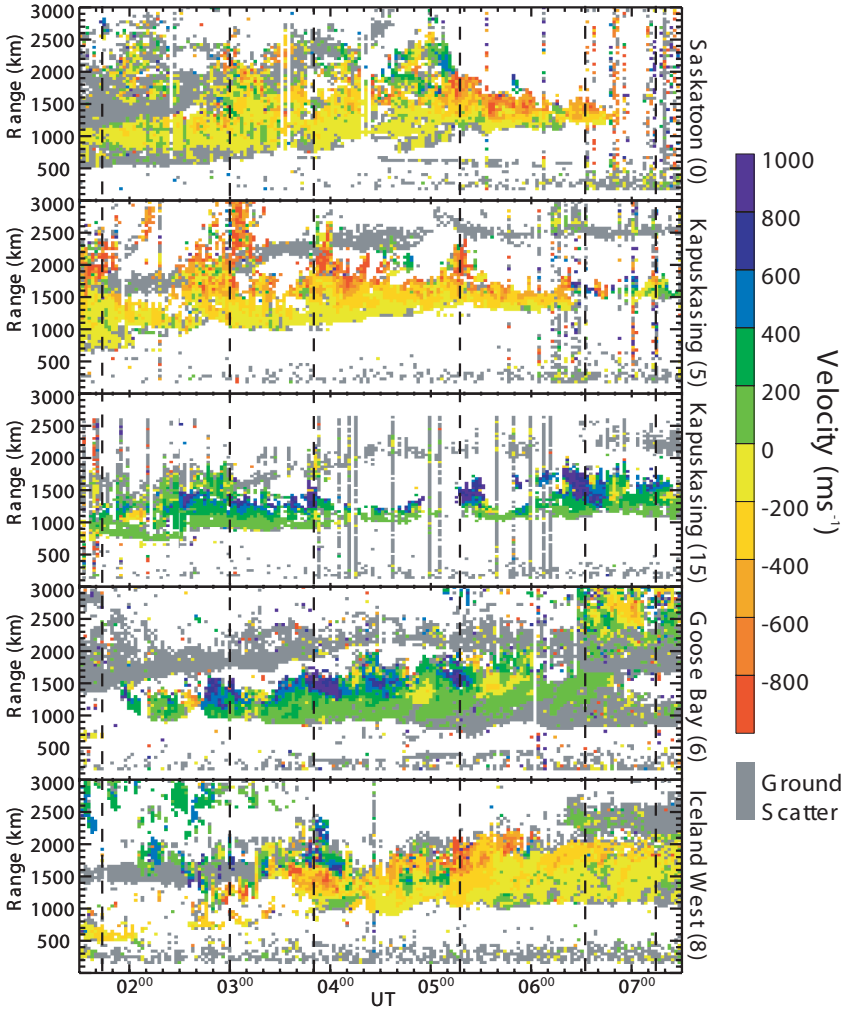

Fig. 3. SuperDARN line-of-sight velocity measurements from the radar beams indicated in Fig. 1a (left side) are shown for the interval 01:30–07:30 UT on 2 Dec 1999. The vertical dashed lines show the centre times of 6 pulsed flow features, which are discussed in detail in the text.

3.1 Upstream interplanetary conditions

In Fig. 2 we present data from the ACE spacecraft, lagged by 76 min via the method described above, for the 18-h interval from 19:30 UT on 1 December to 13:30 UT on 2 December 1999. This is an expanded interval describing the upstream interplanetary conditions for 6 h on either side of the interval of specific interest, which is delimited by the vertical dashed lines. The top two panels show the solar wind proton number density (n_p) and speed (v_p) from ACE/SWEPAM. Data were unavailable for the ∼3-h period, ∼03:30–06:30 UT, as indicated above, so data from the Geotail CPI instrument has been used to fill the gap (indicated on Fig. 2 by the dashed lines). Before the data gap, the density remained relatively constant at ∼10 cm^{-3} and the velocity between 330–380 km s^{-1}. The Geotail data indicates a decrease in velocity of ∼30 km s^{-1} approximately coincident with the SWEPAM data dropout. The middle three panels show the GSM components of the IMF from ACE/MAG, with the magnitude and clock angle of the field shown in the bottom two panels. IMF B_x was near zero or positive throughout the main interval of interest, while B_y was large and negative, and B_z predominantly positive (and had been near zero or positive for more than 3 h previously). These values translate to a field strength which was nearly constant at ∼10±1 nT, and a clock angle which, for the most part (∼02:30–06:30 UT), remained near ∼−60°. The mean value over the main interval was −59°, with a standard deviation of 17°.

3.2 SuperDARN flow data overview

In Fig. 3 we present line-of-sight SuperDARN velocity data for the 6-h interval, from the five radar beams shown by the red lines in the left-hand map in Fig. 1a. These beams have been chosen for their good backscatter returns, as well as for their wide coverage of the nightside ionosphere. Immediately evident is the continuous flow observed over the entire interval, with speeds of ∼500–1000 m s^{-1}. These flows are directed away from the radar at Saskatoon (beam 0) and Kapuskasing (beam 5), indicative of sunward "return" flow in the dusk convection cell, towards the radar at Kapuskasing (beam 15) and Goose Bay (beam 6), indicative of anti-sunward flow over the polar cap into the auroral zone, and

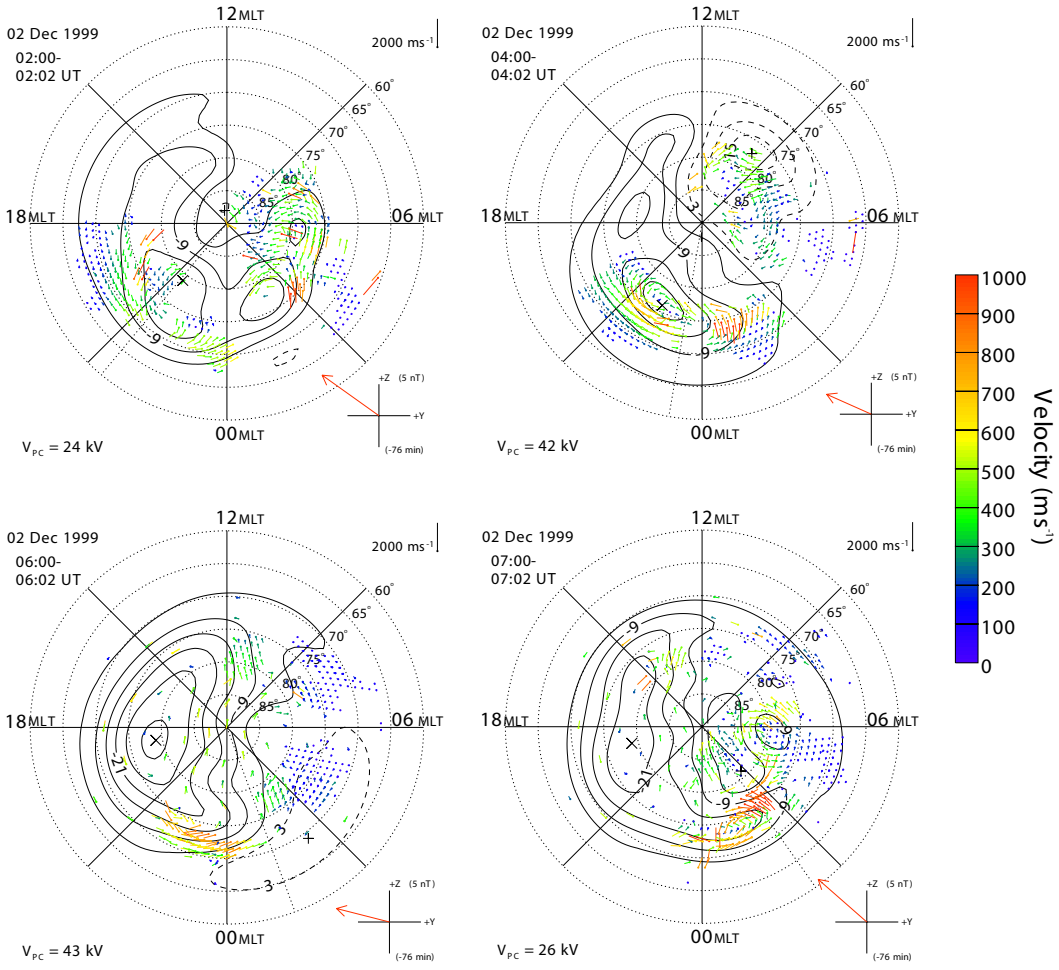

Fig. 4a. Streamlines and vectors of the ionospheric flow derived from the SuperDARN velocity measurements shown on geomagnetic grids, obtained from the "Map-Potential" algorithm (see Sect. 2.1). Four maps are shown from the first 6-h interval studied here for **(a)** the six Northern Hemisphere radars and **(b)** the four Southern Hemisphere radars. Maps are shown at 02:00, 04:00, 06:00, and 07:00 UT for the Northern Hemisphere, and 02:04, 03:00, 04:08, and 05:00 UT for the Southern Hemisphere. At the bottom of each map the total transpolar voltage V_{PC} (left-hand corner), and the direction and magnitude (in the $Y - Z$ plane) of the lagged IMF (right-hand corner) are indicated (Fig. 4 continues).

strong but variable (directed mainly east-west) at Iceland West (beam 8). There is also evidence of strong variability or pulsing in the flow, which is particularly marked, for example, at Goose Bay (beam 6). The vertical dashed lines indicate six such "pulsed" features in the flow, the details and timing of which will be discussed below. It is immediately evident that this is an interval of dynamic and often high speed nightside flow.

In order to investigate the nature of the flow further, we have derived a sequence of convection maps from all the available SuperDARN data (in both hemispheres), using the Map Potential model. In Fig. 4a we present four representative examples of the Northern Hemisphere flow pattern, imaged at 02:00, 04:00, 06:00 and 07:00 UT, which employ 2-min resolution data from the six radars indicated in Fig. 1a. The diagram in the bottom right-hand corner of each plot indicates the direction and strength of the concurrent (lagged) IMF projected onto the y–z plane, emphasising again that although these flow data span 5 h of UT, the IMF conditions remained very similar. Correspondingly, although the details vary from plot to plot, the overall flow pattern also remained similar. It can be seen that the convection was consistently dominated by a large crescent-shaped "dusk" flow cell, which spanned the local time interval roughly from noon (the details being inaccessible due to the lack of post-noon dayside data), via dusk into the post-midnight hours. A clear "dawn" flow cell is present only in the map at 04:00 UT, where it is confined essentially to the dayside MLT quadrant between dawn and noon. In general, the dawn sector flows are highly structured and variable, and appear to be essentially absent, for example, at 06:00 UT. The sense of the dawn-dusk flow asymmetry is exactly that expected for Dungey-cycle flow driven in the presence of strong and consistent negative IMF B_y (Jørgensen et al., 1972; Cowley, 1981; Reiff and Burch, 1985; Heppner and Maynard, 1987; Weimer, 1995; Ruohoniemi and Greenwald, 1996). In par-

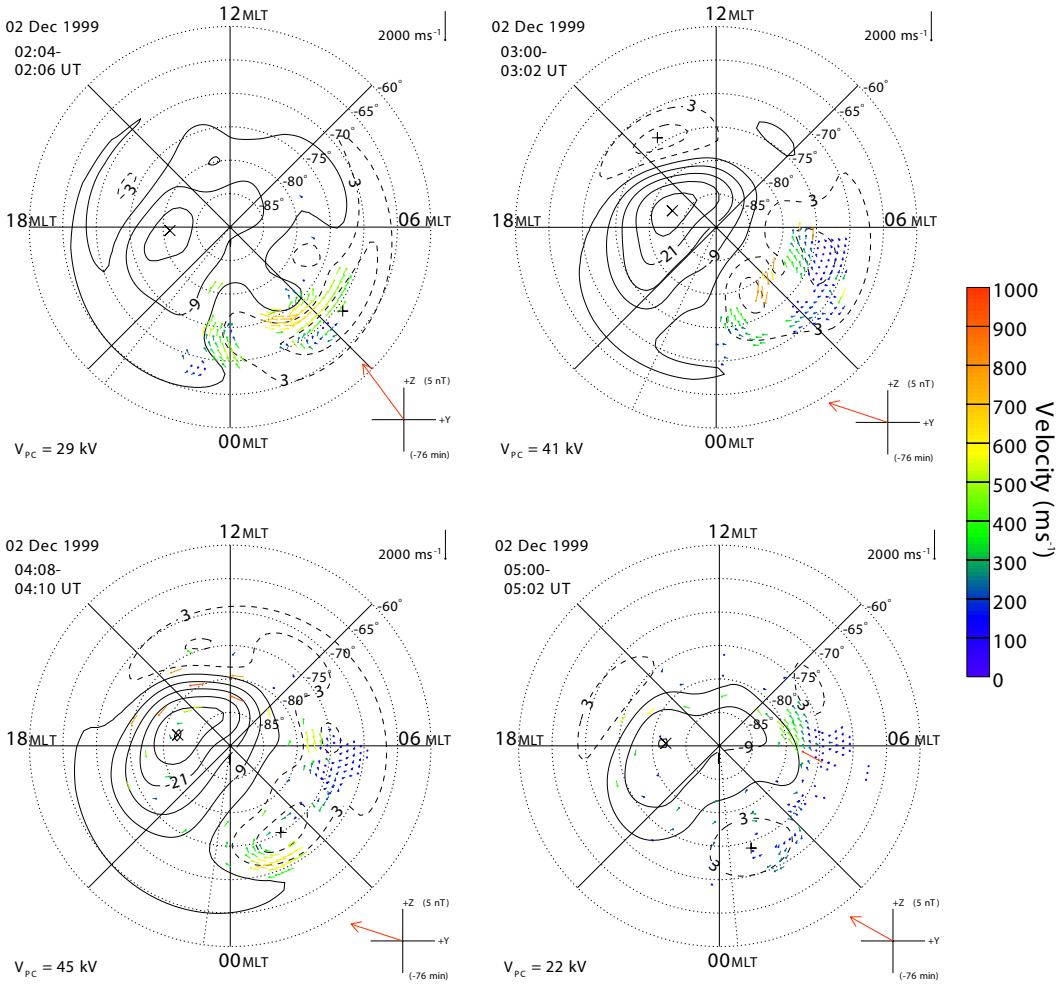

Fig. 4b.

ticular, the predominant sense of anti-clockwise vortical flow within the polar cap, giving faster antisunward flows at dusk than at dawn, is that expected to be produced by the east-west field tension effect on open field lines, which pulls newly-reconnected field lines within the dayside cusp eastward into the dusk sector. Despite the northward direction of the IMF, there is little evidence in these maps for the concurrent presence of high-latitude "lobe" convection cells. However, as mentioned above, the lack of data coverage in the post-noon dayside quadrant makes this statement less than definitive.

If the Northern Hemisphere convection is due principally to IMF B_y-asymmetric Dungey-cycle flow, we would expect to observe similar flows in the Southern Hemisphere, but with an oppositely-directed asymmetry between dawn and dusk. Examination of the Southern Hemisphere data shows that the coverage is much more restricted than in the north, and backscatter is essentially absent after ~06:00 UT. Therefore, in Fig. 4b we show four selected maps from earlier in the interval, at 02:04, 03:00, 04:08, and 05:00 UT, chosen to optimise the coverage. In order to aid comparison, these maps are drawn as though viewed from the north, i.e. with noon at the top and dusk to the left. Although the data are restricted, they are nevertheless compatible with a flow asymmetry which is opposite to that which occurs in the north. In particular, the data suggest the continuous presence of strong antisunward and westward flows in the post-midnight and dawn sector polar cap, in a region where the Northern Hemisphere flows are more sporadic but generally directed eastwards.

As a further check on the nature and origin of the flow patterns, we have also examined all available DMSP particle data and VIS auroral imagery during the interval, in order to determine the nature of the concurrent particle precipitation patterns (though, as noted above, VIS images are available only until ~03:00 UT). On the basis of the above interpretation, we would expect the central region of the convection patterns where the flow is directed antisunward but with an anti-clockwise vortical twist (in the Northern Hemisphere) to correspond to open field lines with cusp/mantle (on the dayside) or polar rain (on the nightside) precipitation, while the surrounding region at lower latitudes should correspond to closed field lines with trapped BPS/CPS pre-

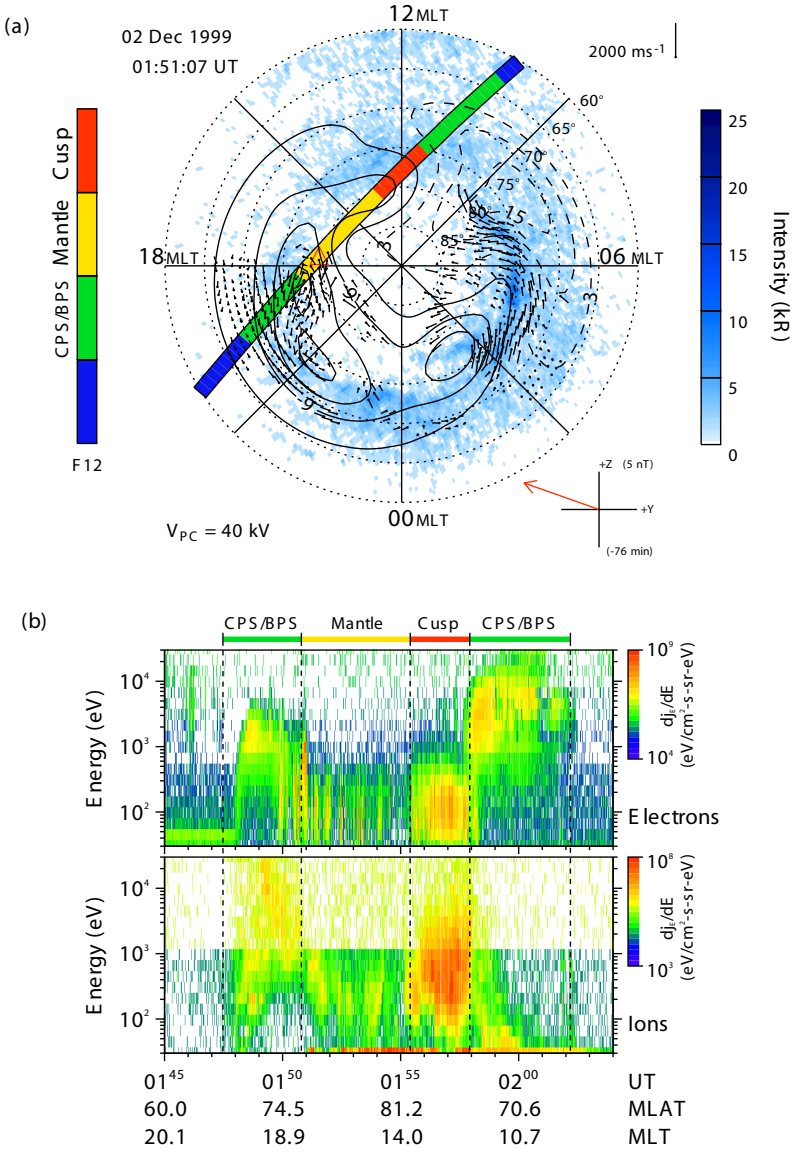

Fig. 5. (a) A map of the UV auroral intensity at 01:51:07 UT (the centre time of the 32.5 s integration interval of the UV image) projected onto a geomagnetic grid. Superposed on this image are SuperDARN "Map-Potential" streamlines and flow vectors, and the orbital track of the DMSP F12 spacecraft from 01:45-02:04 UT, colour-coded to the different regions of particle precipitation (the red triangle indicates the footprint of the spacecraft at the time of the UV image). Also indicated on the map is the derived total transpolar voltage and the direction and magnitude (in the $Y - Z$ plane) of the lagged IMF, as in Fig. 4. The superposed SuperDARN vectors correspond to the two-minute interval which encompasses the centre time of the UV image. **(b)** Standard precipitating particle spectrograms from the SSJ/4 instrument on board the DMSP F12 spacecraft for the overpass shown in (a). Electron (top panel) and ion (bottom panel) data are presented for 01:45–02:04 UT. Also indicated at the bottom of the figure is the magnetic latitude (MLAT) and magnetic local time (MLT) at corresponding universal times (UT).

cipitation (e.g. Newell et al., 1991, 1996). We find that all the DMSP and VIS data are compatible with these expectations. An example is shown in Fig. 5, taken from early in the interval, when VIS images were available, together with a simultaneous DMSP (F12 satellite) overpass. Figure 5a shows the Northern Hemisphere SuperDARN flow vectors and Map Potential flow streamlines for the two-minute scan 01:50–01:52 UT, in the same format as Fig. 4. This is superimposed on a simultaneous VIS image of the UV auroras, obtained over a 32.5 s integration centred on 01:51:07 UT. The intensity of the UV emission is indicated in the bar on the right-hand side of the figure. The VIS data show a central region of almost no emission, which agrees well in location with the region of antisunward and anti-clockwise vortical flow in the convection map. We take this central region to be the region of open magnetic flux. Surrounding this, a near-circular continuous ring of emission is observed, due to precipitating ∼keV electrons, which generally closely coincides with the region of clockwise flow in the extended crescent-shaped "dusk" convection cell. We take this region to correspond, to

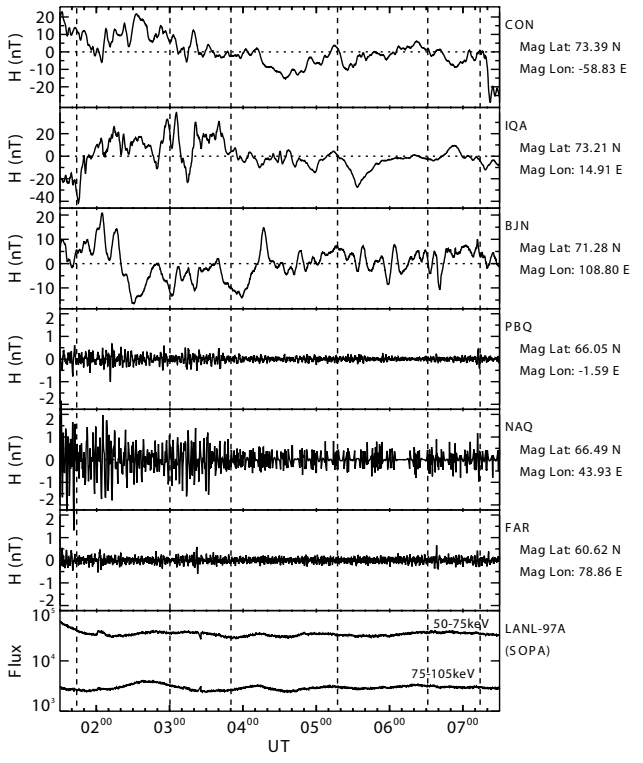

Fig. 6. The upper three panels show H-component magnetic field measurements from the blue colour-coded array in Fig. 1b, for 01:30–07:30 UT on 2 Dec 1999. Panels 4–6 show filtered (20–200 s) H-component magnetic field measurements from the low-latitude magnetometer array (red dots in Fig. 1b) for the same interval. The bottom panel shows geostationary electron fluxes in two energy channels (50–75 keV and 75–105 keV) from the SOPA instrument on the LANL97A spacecraft. The vertical dashed lines correspond to those in Fig. 3.

a first approximation, to the region of trapped hot plasma on closed flux tubes.

Figure 5a also shows the track of the DMSP F12 spacecraft as it passed over the polar regions during the interval 01:45–02:04 UT. The spacecraft position at the centre time of the VIS image (and also very nearly the centre time of the SuperDARN scan) is indicated by the red triangle. The track is colour-coded by the nature of the precipitation observed, i.e. CPS, BPS, cusp, and mantle. The data on which these classifications are based are shown in standard spectrogram format in Fig. 5b. It can be seen that the regions designated as CPS/BPS lie within the region of UV auroral emission, and sunward or clockwise vortical flow. The region of "mantle" precipitation corresponds to the central region of weak emission, and antisunward and anti-clockwise flow in the post-noon sector, while the "cusp" precipitation, taken to be indicative of newly-opened dayside field lines, extends across the poleward boundary of the UV emission near noon, in the region where the Map Potential streamlines turn poleward and eastward. Overall, these data (and those obtained in other VIS images and on other DMSP passes) provide significant support for our interpretation of the observed flows as asymmetrical Dungey-cycle convection patterns driven by dayside and nightside reconnection. In particular, the cusp/mantle precipitation observed by DMSP on the pass displayed here in itself constitutes direct evidence of ongoing dayside reconnection.

The data in Figs. 3–5 are thus indicative of the essentially continuous presence of flow driven by open flux tube production at the magnetopause and destruction in the tail during the interval. It is then important to emphasise that the approximately constant size of the flow patterns seen in Fig. 4 implies an approximate balance in the dayside and nightside reconnection rates over the interval as a whole. It can be seen, for example, that the flow reversal boundary and implied open-closed field line boundary near midnight stays within a few degrees of $\sim 75^\circ$ through the entire interval. Judging from the position of this boundary at various local times, the amount of open flux present in the system is typically $\sim 4 \times 10^8$ Wb (see later for more detailed estimates). The mean transpolar voltage for the entire interval was 35 kV, corresponding, of course, to a magnetic flux throughput in the flow system of ~ 35 kWb s^{-1}. If this flow was associated with essentially unbalanced dayside reconnection and open flux production, the amount of open flux that would be created over the 6 h interval (across a small merging gap) would be $\sim 8 \cdot 10^8$ Wb, thus essentially tripling the amount of open flux present in the system. Clearly this does not happen. Similarly, if the flow was associated with essentially unbalanced nightside reconnection at this rate, the polar cap would contract to zero size in ~ 3 h. Clearly this also does not happen. (In addition, we would not expect the IMF B_y-associated flow asymmetry to persist in this case.) Rather, if we set a rough limit for the change in open flux over the interval of say, $\sim 1 \cdot 10^8$ Wb, corresponding to a change in the overall boundary position of $\sim 2^\circ$, the implied difference in the dayside and nightside reconnection rates averaged over the 6 h of the interval is ~ 5 kV, small compared with the overall voltages deduced from the flow of ~ 35 kV. The flow maps thus imply approximate balance between dayside and nightside reconnection rates, averaged over the whole interval, to within 10–15%. However, as we will show below, this does not imply that detailed balance occurs throughout, as the pulsed nature of the nightside flows noted above already suggests.

3.3 Overview of substorm indicators

Given the implied existence of nightside reconnection at an appreciable averaged rate during this interval, it is of interest to enquire whether this process is expressed in terms of substorm expansions, as is characteristic of intervals of southward-directed IMF. Data relevant to this issue are summarized in Fig. 6. The top three panels present *H* component magnetograms from the azimuthal magnetometer array at $\sim 71^\circ$–73° latitude (colour-coded blue in Fig. 1b), which we examine for the presence of magnetic signatures, indicative of the formation of substorm electrojets. These stations

are at a higher latitude than those at which substorm expansion onsets usually occur during or directly after intervals of southward IMF (∼65°), but they are relevant in the present context in view of the contracted nature of the flow patterns displayed in Figs. 4 and 5. We also confirm that they are representative of all the data from all the networks surveyed in this study. These data show that the geomagnetic field was "quiet" during the whole interval, with no indications of impulsive substorm activity. Field variations were continuously present on time scales of several tens of minutes, but the amplitudes were typically only a few tens of nT. There is some evidence of a relationship between these variations and those in the flow, marked by the vertical dashed lines, as in Fig. 3, and this will be discussed later.

The lack of impulsive substorm-like activity is emphasized in the next three panels of Fig. 6, which show representative magnetic field data from lower-latitude stations (colour-coded red in Fig. 1b), which have been filtered between 20–200 s, corresponding to the Pi2 band. None of these data (including those from stations not shown here) indicate any impulsive substorm-like Pi2 features, though the data from NAQ does indicate some continuous activity of amplitude ∼1 nT during the first ∼2 h of the interval. However, there does not appear to be any detailed correspondence between this low-level activity and the times of the flow features discussed above. Finally, the bottom panel of the figure shows representative data from the geostationary energetic particle monitors, specifically two channels of energetic electron data from spacecraft LANL97A, located in the dawn sector (see Fig. 1b). Small periodic flux variations are evident over the interval, but no injection signatures are present, or any obvious relationship to the flow features, as is indeed the case in the data from all the LANL spacecraft. Thus, if particle injections from the tail did occur, they did not reach geostationary orbit. Overall, therefore, we summarize our findings by stating that no indications of substorm bays, Pi2s, or geostationary orbit particle injections were observed during the interval. The tail reconnection which occurred was, therefore, not manifest as classic near-Earth substorm expansions. Nevertheless, impulsive activity was indeed observed in the nightside flow, as noted above, and in the next section we turn to examine its behaviour in more detail.

3.4 Nightside flow bursts

We now examine more closely the variability of the nightside flow, whose presence is already indicated in the data presented in Figs. 3 and 4. In Fig. 7 we extract parameters from the Map Potential plots which provide measures of the variability of the flow. The top panel shows the total transpolar voltage in the flow maps, representing a measure of the total flux transport in the flow system. The level of confidence in this parameter in general depends on the coverage of the polar ionosphere by the radar data. Examination shows that during this interval the data generally do span the extrema in the voltage values (see, e.g. Fig. 4), so that we may have reasonable confidence overall. It can be seen that the voltage values

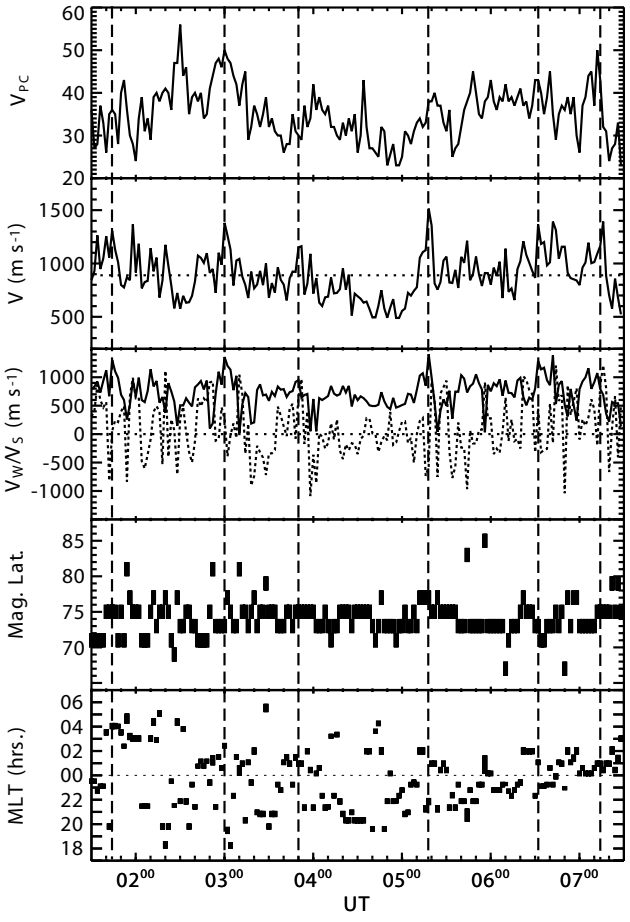

Fig. 7. Flow measurement time series obtained from the SuperDARN radar observations and the "Map-Potential" algorithm. The top panel shows the total transpolar voltage, V_{PC}. The second panel shows the peak nightside ionospheric flow speed (the horizontal dotted line is the average over the interval), and the third, the north-south (dotted line) and westward (solid line) components of the peak flow. The bottom two panels show the location of this peak flow in magnetic latitude (fourth panel) and MLT (bottom panel). The vertical dashed lines indicate six peaks in the flow speed, corresponding to those in Figs. 3 and 6.

lie typically between ∼25 and ∼50 kV, and exhibit intervals of relatively steady values close to the mean of 35 kV, interspersed at roughly 1-h intervals with enhancements lasting ∼10–15 min during which the voltage increases up to peaks of ∼40–50 kV.

Inspection of the flow maps shows that these enhancements are manifest as localized bursts of fast flows, generally located in the westward "dusk" cell flow spanning the midnight sector. The second panel of Fig. 7 then shows a complementary measure of the flow variations, namely the peak nightside flow speed, occurring in each 2-min Map Potential plot specifically in these westward "return" flows. In order to provide a representative value, we have averaged the vector velocities in bins which are 220 km square, corresponding to 2° latitude and typically ∼7° longitude, representing four "pixels" of the Map Potential algorithm. Again,

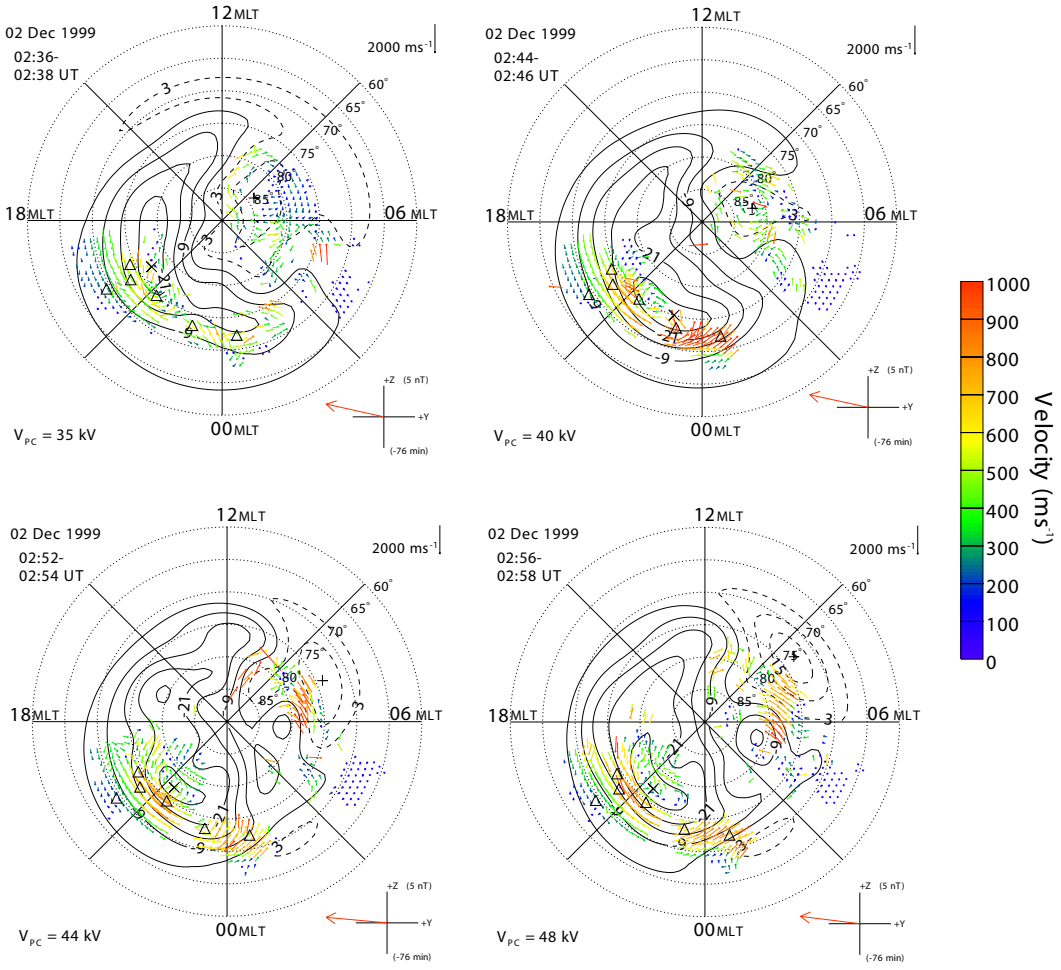

Fig. 8a. Flow maps illustrating the flow "bursts" indicated by the vertical dashed lines in Fig. 7, shown in the same format as Fig. 4. Eight selected maps are shown for each of the two burst intervals **(a)** 02:36–03:20 UT and **(b)** 05:02–05:30 UT. The exact time of each 2-min map is indicated in the top left-hand corner. Maps corresponding to the centre times of each of the other four bursts are shown in **(c)**. Also indicated on the maps by the black triangles are the locations of the magnetometer stations colour-coded yellow in Fig. 1b (Fig. 8 continues).

the bursty nature of the flow is evident. Typical values of $\sim$500–800 m s^{-1} are interspersed with $\sim$10–15 min bursts, reaching up to $\sim$1500 m s^{-1}. The averaged value of the peak flow speed over the interval, 891 m s^{-1}, is indicated by the horizontal dotted line in this panel, emphasizing the peaks in the flow. The most prominent and long-lived of these peaks are marked by the vertical dashed lines, these being the same lines as those shown previously in Figs. 3 and 6. Comparison with the data in the upper panel of Fig. 7 shows that most of the peaks in the speed also correspond to a peak in the trans-polar voltage. This indicates that an overall enhancement in the flux transport took place in association with the flow bursts, and not just a reconfiguration in the flow pattern.

The third panel of Fig. 7 shows the vector components of the flow associated with the peak speed shown in the second panel. The solid line shows the westward flow component (perforce positive, since the peak flow speed displayed corresponds specifically to the westward flow of the "dusk" return cell), while the dashed line shows the north-south flow (positive equatorward). These data show that, with the exception of the burst peaking at 07:16 UT, the peak flows all occur in the westward component. Concurrent changes in the north-south component are also observed, however, with enhancements in the equatorward component often occurring in the vicinity of the peak in the westward flow. The lower two panels of the figure also show the magnetic latitude and MLT of the location of the peak flow speed. It can be seen that the latitude of the peak flow is generally located in the range 73°–75°, and shows little trend during the interval, consistent with our previous discussion concerning the lack of overall change in the size of the flow system. Similarly, the local time of the peak flow speed is scattered $\sim$2–3 h on either side of midnight, and also shows no overall preference or trend.

3.4.1 Flow burst geometry

Having investigated the overall nature of the nightside flow data, we now examine in more detail the nature of the flow variations which occur in two of the flow bursts, those centred near (and indicated by the vertical lines at) 03:00 and

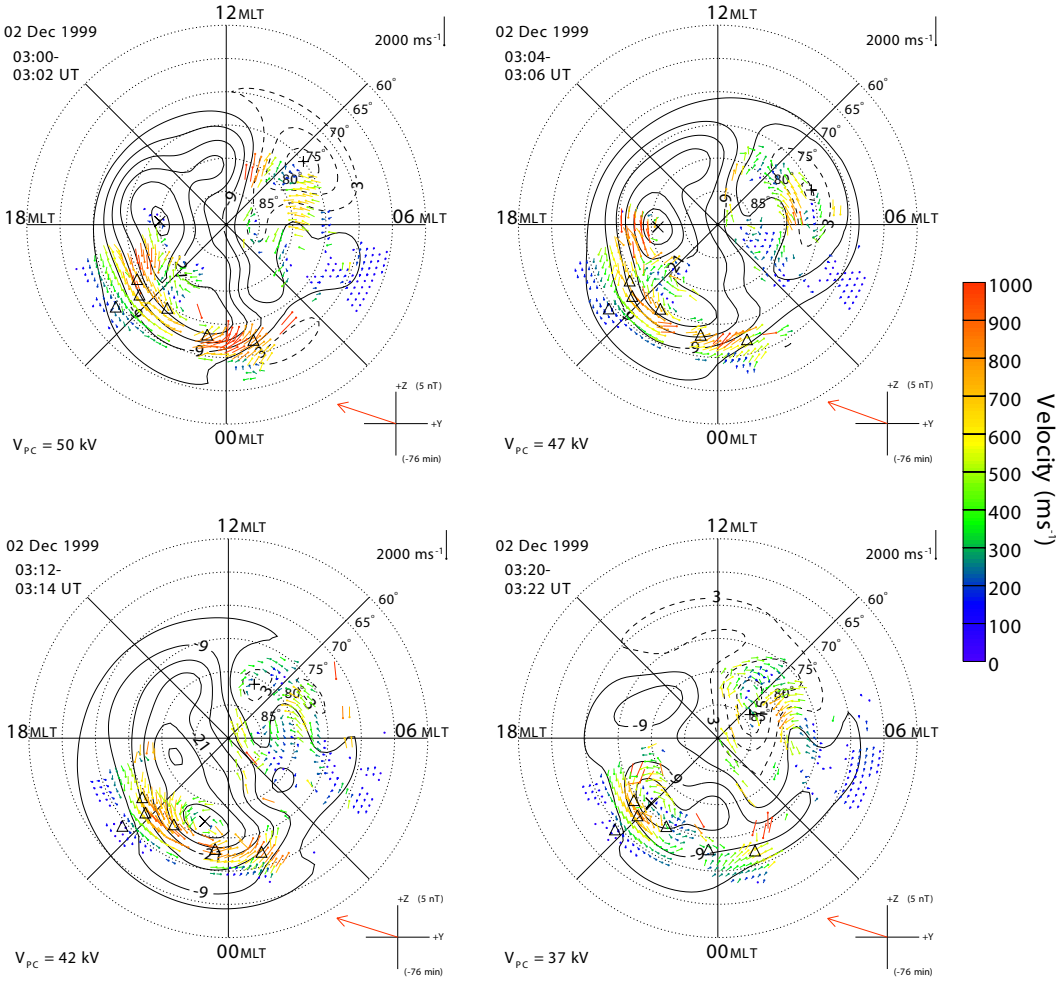

Fig. 8a. ... continued.

05:18 UT. Figure 8a shows eight selected 2-min flow maps which span the first of these intervals, between 02:36 and 03:20 UT. The black triangles in these plots show the positions of key ground magnetometer sites whose data will be examined below. The first map, for the 2-min interval starting at 02:36 UT, is illustrative of the nature of the flow over the previous ∼20-min interval. It shows a well-formed IMF B_y-asymmetric flow pattern of modest intensity, in accordance with the overview presented above, with a well-developed crescent-shaped "dusk" flow cell stretching from noon via dusk to the post-midnight hours, together with a weaker rounder "dawn" flow cell which is centred in the pre-noon sector. The transpolar voltage is estimated to have been 35 kV. Over the next ∼15 min, the dusk cell flow then grew in magnitude, with fast equatorward flows near midnight, and fast westward "return" flows in the pre-midnight sector, which eventually extended to the edge of the radar field of view at ∼19 MLT. The transpolar voltage reached 44 kV at 02:52 UT, and remained at around that value for the next ∼20 min. Rapid equatorward and westward flows were also observed in the dawn sector after this time, which, bearing in mind the asymmetric nature of the flow pattern, could also have been connected with the enhancements observed closer to midnight. The flow magnitude fell rapidly after 03:12 UT, however, such that the transpolar voltage reduced to values of ∼35 kV by 03:20 UT, similar to that occurring before the burst.

Figure 8b shows in the same format the development of a second flow burst during the interval from 05:02 to 05:30 UT. The first map, starting at 05:02 UT, shows a weak flow pattern with a transpolar voltage of 31 kV, which is dominated by clockwise vortical "dusk" cell convection. The "return" flows in the pre-midnight sector were relatively strong, however, as had been the case for the previous ∼20 min. These flows persisted until ∼05:06 UT, when an enhancement began in the pre-midnight sector, which developed over the next ∼15 min into a predominantly azimuthal flow feature spanning some 6 h of MLT about the midnight meridian (within the fields of view of the radars), and containing flows which peaked at ∼1500 m s^{-1}. Peak estimated transpolar voltages of ∼40 kV occurred at ∼05:20 UT, the flows then subsequently declining to reach transpolar voltages of ∼30 kV once more after ∼05:30 UT.

Overall, the geometry of these two flow burst events are

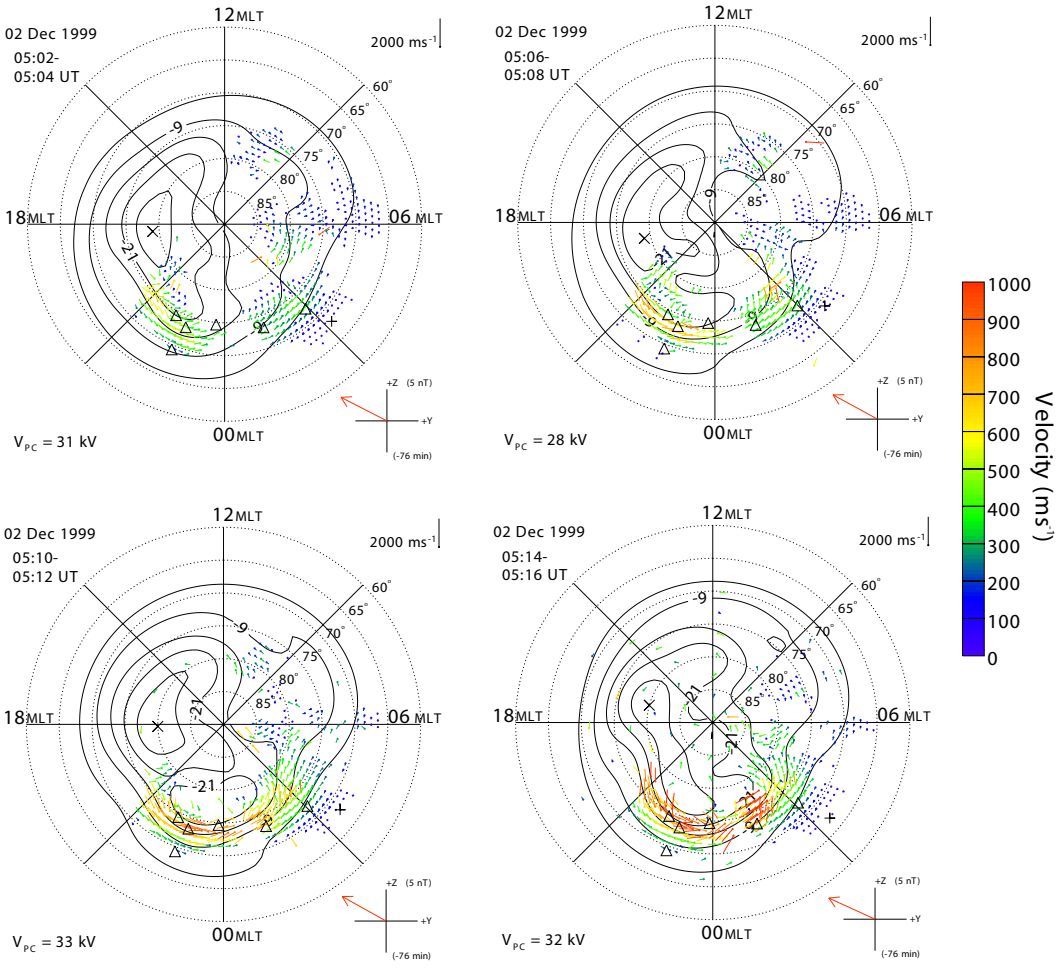

Fig. 8b. ... continues.

seen to be similar to each other, both involving a strong enhancement in the nightside westward dusk cell "return" flow. However, in the second case the region of rapid equatorward flow out of the polar cap appears to have shifted from near midnight into the post-midnight sector, such that the region of enhanced westward flow also moved eastward to span the midnight sector. In Fig. 8c we show a gallery of flow maps taken from the centres of each of the remaining bursts that occurred during the interval, at the times indicated by the vertical dashed lines in Fig. 7. Within the limits of the radar data coverage, each of them displays an enhancement in the westward dusk cell "return" flows in the pre-midnight-to-midnight sector, with enhanced equatorward flows out of the polar cap in the midnight-to-post-midnight sector. The burst centred at 01:44 UT also shows the presence of rapid equatorward flows in the dawn sector, with westward flows extending into the pre-midnight sector, which may be a related phenomenon.

3.4.2 Bursts as nightside reconnection events

The geometry of the flow surges revealed by the above analysis suggests that they are formed by bursts of enhanced reconnection in the geomagnetic tail. If so, we might expect them to be associated with overall poleward contractions in the open-closed field line boundary and in the flow pattern. It is evident from the flow maps shown in Fig. 8 that only in certain cases do the flow data consistently define a sharp flow reversal boundary whose motion can be reasonably clearly followed over the duration of the burst, and then only over a limited local time interval in the pre-midnight sector. It is primarily for this reason that we make the following analysis of just the first of the two bursts discussed above. In Fig. 9 we show data for the interval 02:30 to 03:30 UT. The top panel shows the transpolar voltage obtained from the Map Potential plots, showing the enhancement in the overall flux transport during the burst, while the dashed vertical lines delimit the central ∼30-min interval of enhanced flows. The lower panel shows the latitude of the peak potential in the Map Potential plots in the pre-midnight sector, corresponding to the east-west flow reversal, specifically for 21 MLT (as dictated by the coverage of radar data). These values are quantized in units of 1° by the Map Potential algorithm. Again, the central ∼30 min of enhanced flows are delimited by the vertical dashed lines. The 2–3 points immediately after the burst,

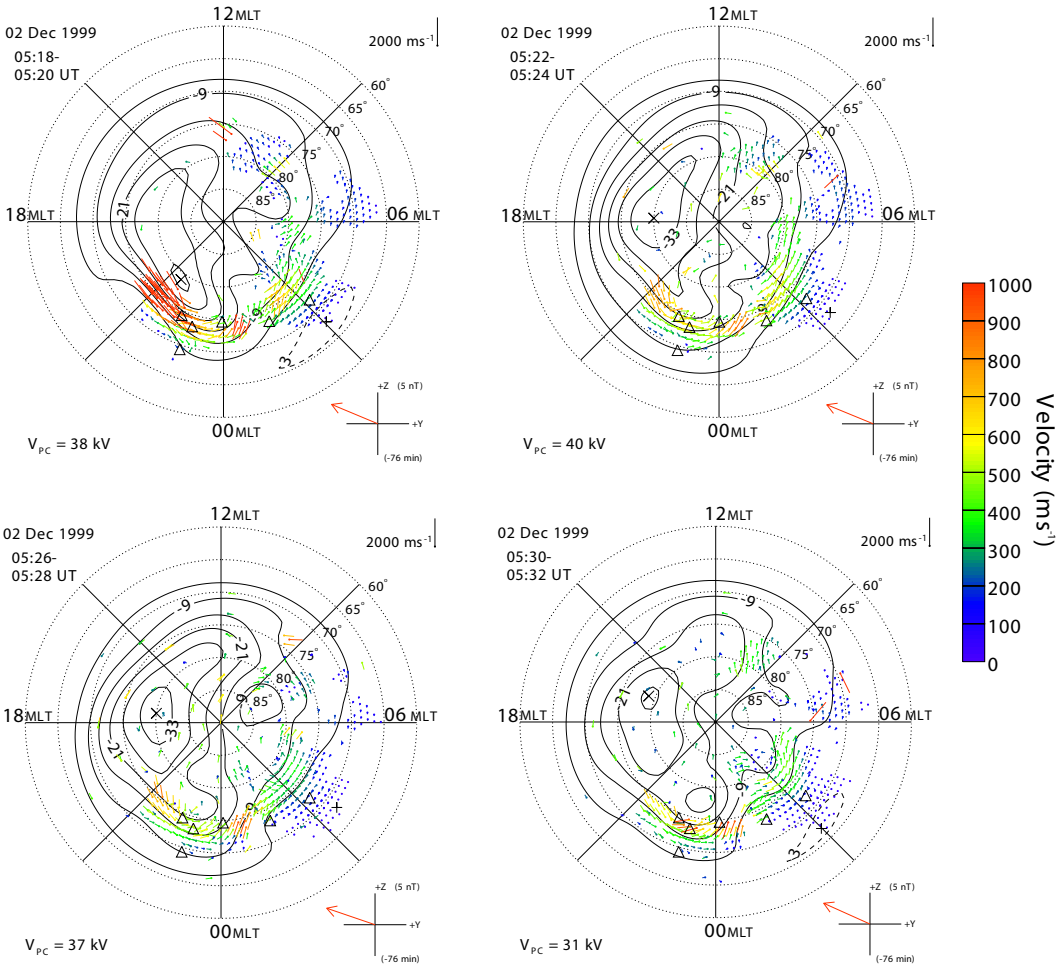

Fig. 8b. ... continued.

which suggest a sudden drop in the latitude of the boundary appear to be associated with an additional, smaller scale flow feature near midnight and are, therefore, unlikely to be representative of the location of the boundary elsewhere. Despite this, and the evident scatter and the quantization, these data do suggest the occurrence of a small poleward contraction of the boundary across the event, by ∼1°–2°, from ∼76° to ∼78°. Extrapolated around the boundary of the polar cap, such a displacement implies a net closure of open flux of $\sim 1 \pm 10^8$ Wb, due to enhanced tail reconnection exceeding the concurrent dayside reconnection rate during the burst interval. The implied difference in rates is by several tens of kV averaged over the duration of the burst. In Sect. 5 below we perform a more detailed analysis and attempt to quantify the dayside and nightside reconnection rates during the burst interval within the limitations of the available data.

3.4.3 Burst magnetic signatures

Although the above data suggest that the observed flow bursts are due to intervals of enhanced reconnection in the tail, we have already demonstrated above that they are not associated with classic substorm features. However, small amplitude fluctuations do occur in the nightside magnetometer data during the interval, and we now investigate the relationship of these variations with those in the flow data. In Fig. 10 we present magnetometer data for each of the two bursts, from the high-spatial resolution array (yellow dots) shown in Fig. 1b. This array is also indicated by the black triangles on each of the flow maps in Fig. 8. For each burst we show the perturbation field superposed with the flow data from the 220 km square bin corresponding to the location of the magnetometer (such that the location of the bin corotates with the station). If the horizontal perturbations are due to overhead Hall currents, then they should correlate with the flow variations according to $\Delta H \propto \Sigma_H V_W$ and $\Delta D \propto \Sigma_H V_N$, where H and D are the northward and eastward components of the magnetic perturbation, respectively (as before), V_W and V_N are the westward and northward components of the flow, and Σ_H is the height-integrated ionospheric Hall conductivity. Such simple relationships will not always hold, particularly in high spatially structured circumstances, due to the integrating nature of ground-based magnetic observations. However, they should be approximately valid here, where the spatial scale for variations in the flow is several

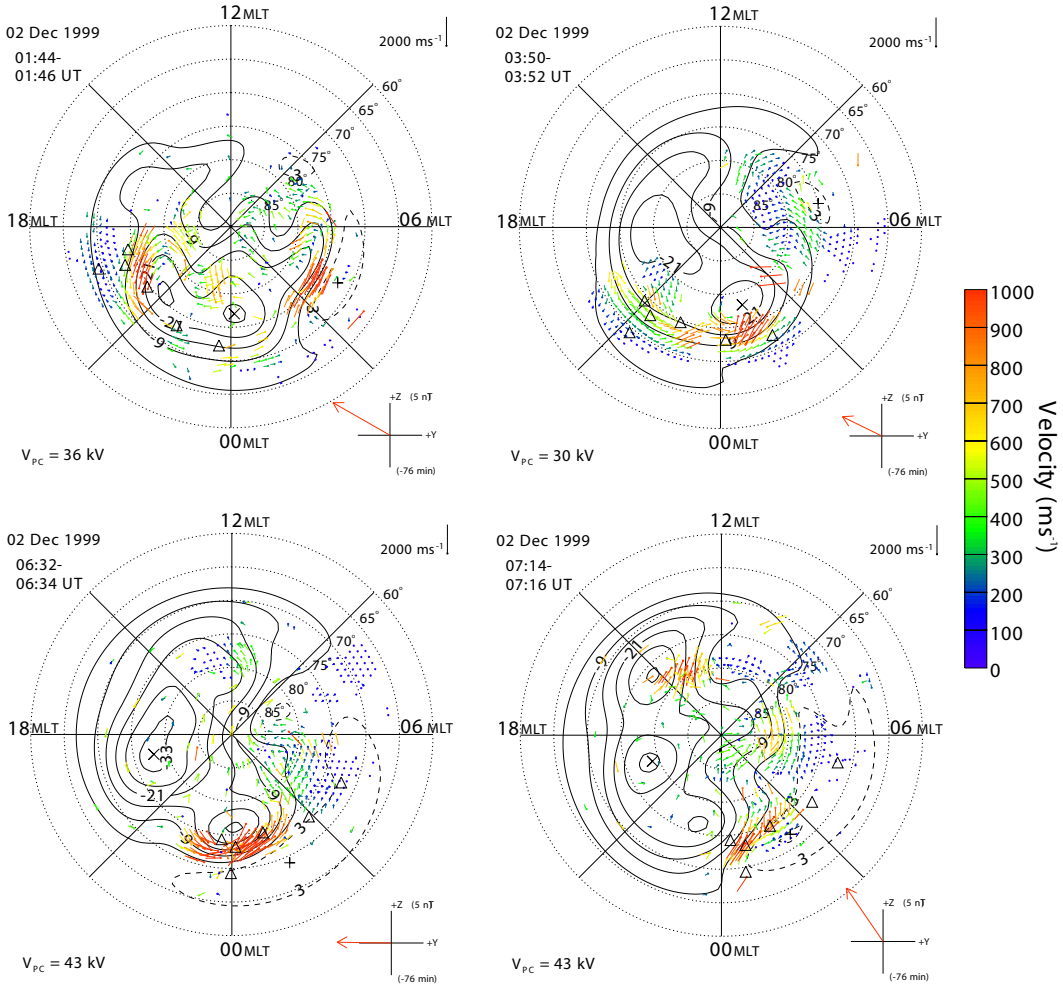

Fig. 8c. see Fig. 8a

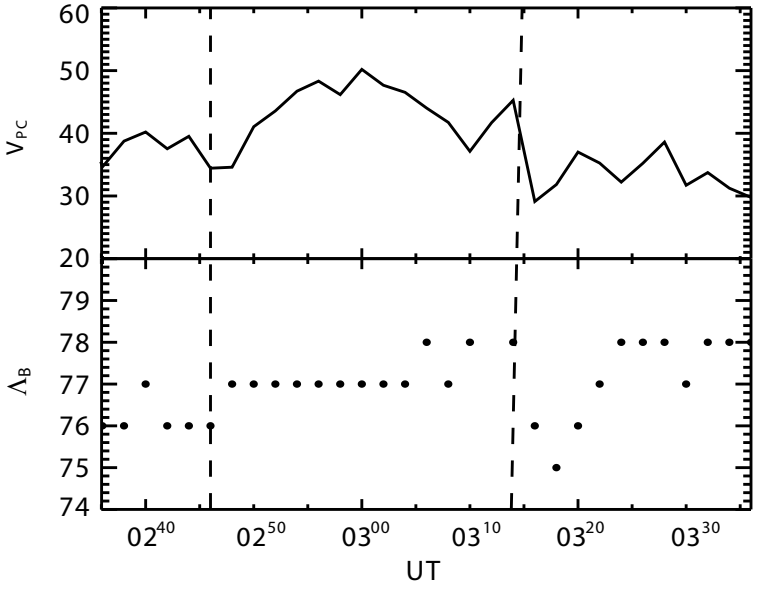

Fig. 9. The total transpolar voltage V_{PC}, derived from SuperDARN radar data using the "Map-Potential" algorithm (top panel) and an estimate of the latitude of the nightside flow reversal boundary (Λ_B) obtained from the minimum in the electrostatic potential (determined at 21 MLT) (bottom panel). Data is shown from 02:36–03:36 UT for the 02 Dec interval. The vertical dashed lines delimit the ∼30-min duration of each burst.

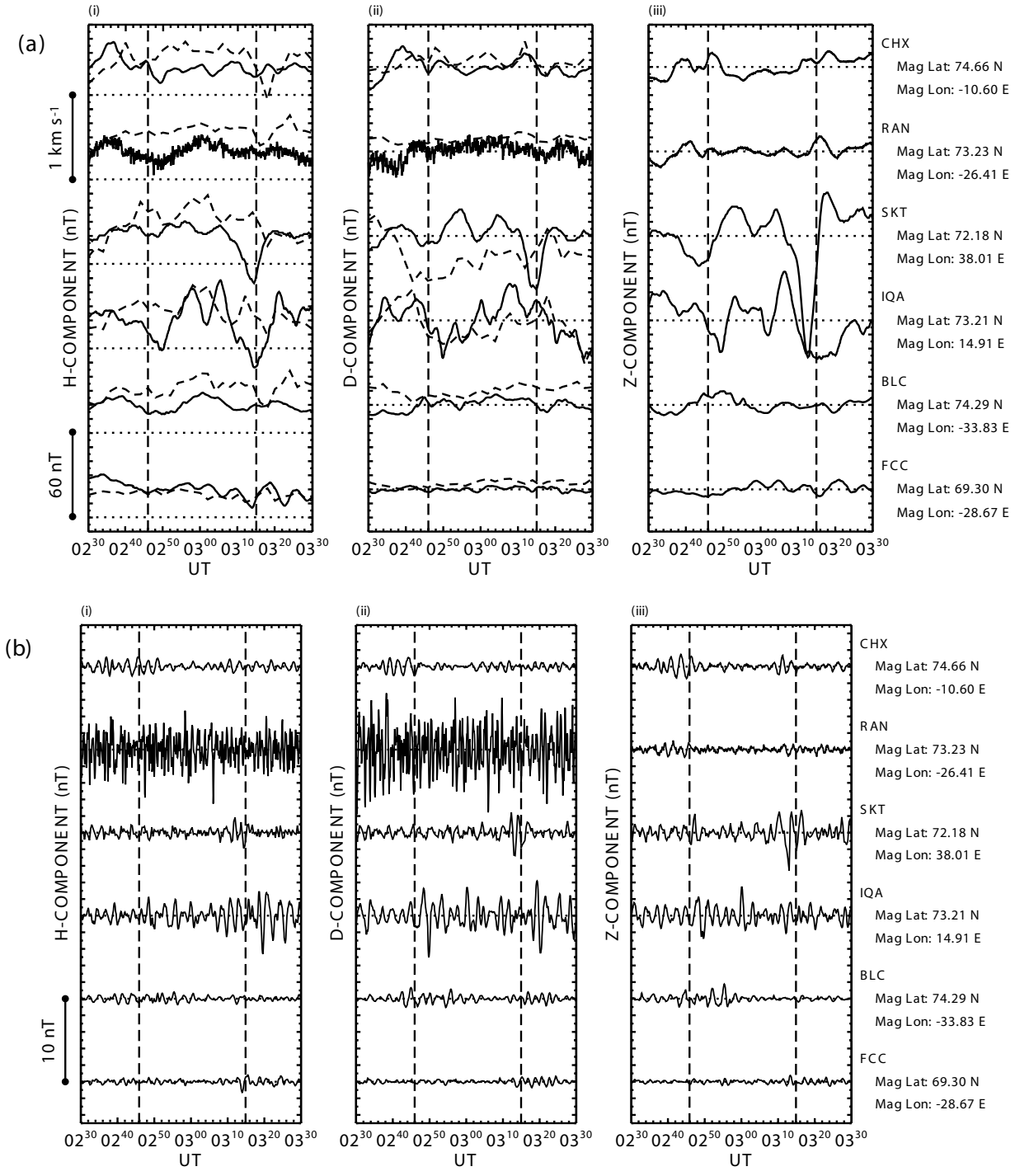

Fig. 10. The H-, D- and Z-components of the ground magnetic field measured by the stations colour-coded yellow in Fig. 1b, and indicated in Fig. 8 by the black triangles. **(a)** The perturbation field (solid lines) for the interval 02:30–03:30 UT on 2 Dec 1999, superposed with the east-west (in (i)) and north-south (in (ii)) SuperDARN flow components (dashed lines) corresponding to the locations of the magnetometers. **(b)** The same magnetic data, band-pass filtered (20–200 s) to highlight Pi2-band activity. **(c–d)** show similar data from 04:40–05:40 UT. The scales to the left of each plot indicate the range between the baselines (horizontal dotted lines) and the vertical dashed lines are as in Fig. 9. (Fig. 10 continues).

100 km as can be seen in Fig. 8. It was noted above that low-amplitude Pi2-band (5–50 mHz) activity was present during the intervals. Therefore, we also show the filtered data from the same stations, to ascertain whether there is any localized activity which might be related to the bursts.

Figure 10a presents the magnetic and flow data for the first burst. In this figure, and in Figs. 10b–d, the vertical dashed lines correspond to those in Fig. 9, delimiting the

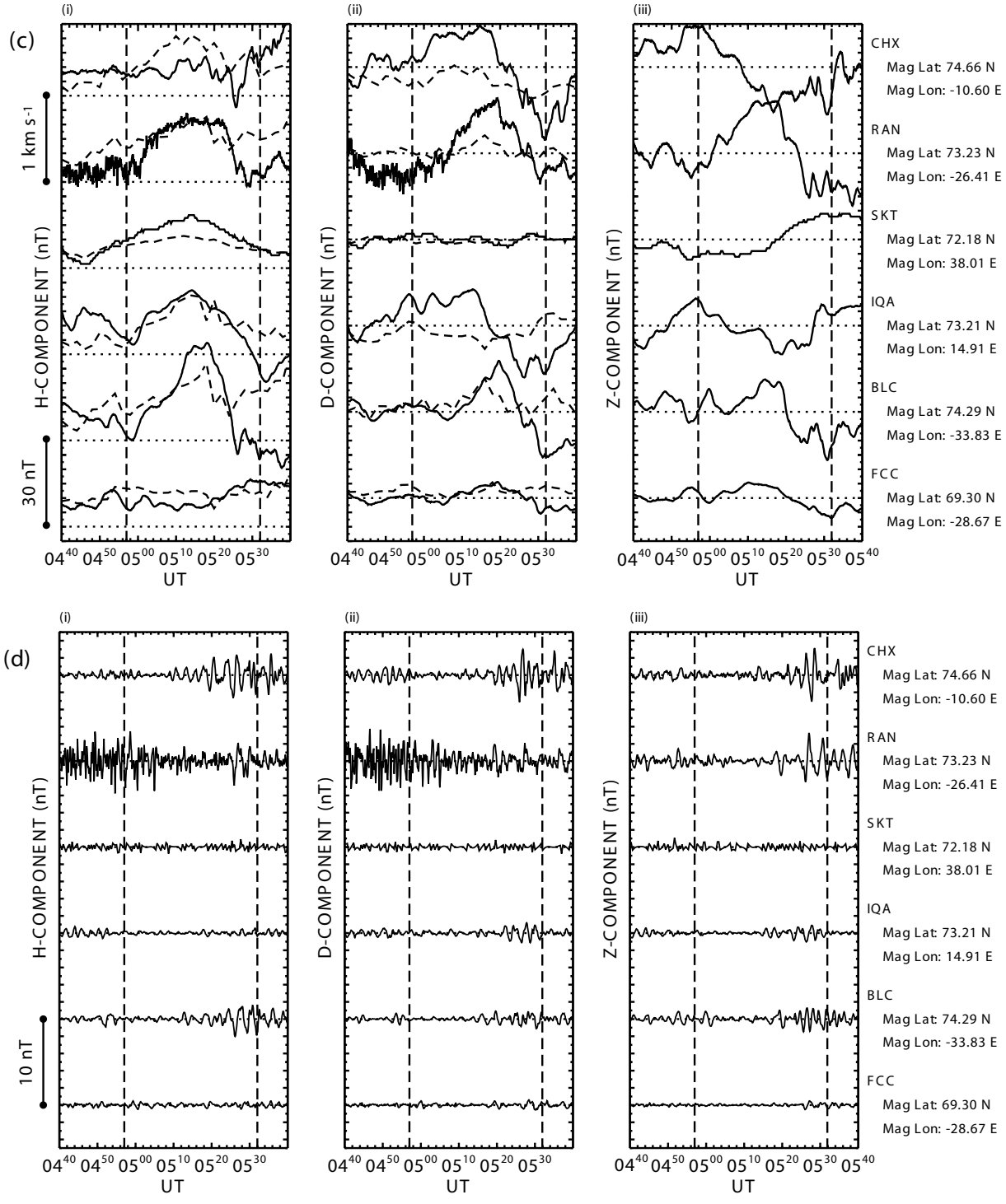

Fig. 10. ... continued.

∼30-min burst duration. Panel (i) contains the H-component magnetic field data (solid line), and the overhead westward component of the flow (dashed line), as discussed above. Although the two curves do not agree everywhere, certain features are present in both data sets. For example, an enhancement in the flow at the location of BLC is accompanied by an increase in the local H-component. In panel (ii), which contains the D-component magnetic field data and the similarly-corresponding northward component of the flow (dashed line), there is also some correlation between the two. For example, the enhanced equatorward flows seen at the location of IQA are accompanied by a coincident negative bay in the field. If we take values of $\sim$1000 m s^{-1} for the flow speed, and magnetic perturbations of $\sim$50 nT, then the im-

plied value of Σ_H is just a few mho. Although as indicated above, it can in general be dangerous to relate local fields and flow in this way; we can confirm that only low-amplitude magnetic effects were observed over the whole array of stations examined here. This, together with the general lack of consistent correspondence between the field perturbations and the flow, suggests that the auroral precipitation during these events within the region of enhanced flow was very low, certainly by comparison with substorm intervals. Finally, panel (iii) contains the Z-component magnetic field data which show similar fluctuations to the other two components and a large negative deflection at ∼03:10 UT. This feature can also be identified in the H- and D-components, but has no clear signature in the flow data.

In Fig. 10b we show the same magnetometer data bandpass filtered between 20–200 s, as discussed above. Station RAN measured the largest amplitude activity in the H- and D-components, but this does not appear to be related to the time of the burst. At CHX, IQA, and BLC, however, there is some evidence of enhanced activity during the burst, although this is of a more continuous nature, unlike the impulsive Pi2-signatures typical of substorms.

Figures 10c and d present data in the same format for the second burst. The magnetometer and flow data in Fig. 10c show similar trends to those for the first burst, although there now appears to be a rather clearer correlation between the two data sets in this case. This is particularly evident in the H-component magnetometer and east-west flow data. Again, the amplitudes of the correlated perturbations are such that the values of Σ_H implied by these data are no more than a few mho, suggesting that, as in the previous example, no strong conductivity changes are present and hence, no strong precipitation. Figure 10d shows the filtered (20–200 s) magnetometer data for this burst. The general picture is much the same as for the first burst, with some small amplitude activity observed at certain stations. In particular, there appears to be a well-defined "onset" of low-amplitude activity observed at CHX and BLC associated with the central time of the burst, at ∼05:18 UT.

3.5 Interval 1 summary

We now summarize our main findings. During this interval, in which an IMF clock angle of $\sim -60°$ was maintained for ∼6 h, dayside reconnection continued to drive Dungey-cycle flow in the magnetosphere-ionosphere system. It is found that, over the entire interval, the size of the convection pattern remained relatively constant, implying that tail reconnection was also ongoing, at an average rate approximately equal to that on the dayside. However, the usual substorm cycle did not occur, evidenced by the lack of magnetic bay signatures at high latitudes, Pi2 signals, and geostationary orbit energetic particle injections. Instead, ∼1000 m s^{-1} bursts of flow were observed in the nightside ionosphere, lasting a few tens of minutes and recurring every hour or so, accompanied by weak magnetic signatures and low amplitude Pi2-band (5–50 mHz) activity. One burst studied in detail, for which there was a well-defined flow reversal boundary in the flow data, appeared to coincide with a ∼1°–2° contraction of the boundary. Thus, these data indicate that the bursts are associated with intervals of enhanced tail reconnection, during which the tail reconnection rate temporarily exceeds the dayside reconnection rate.

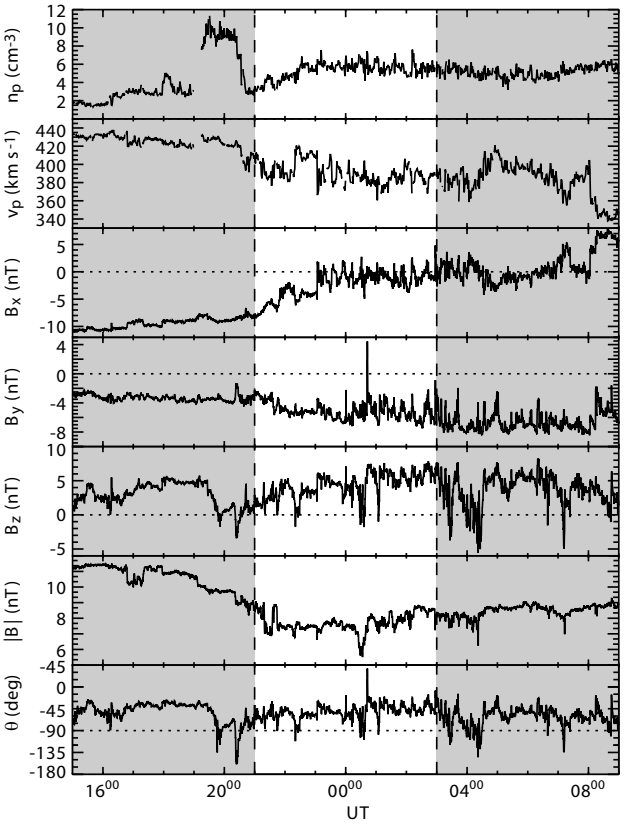

Fig. 11. Upstream interplanetary observations as in Fig. 2 for 15:00 UT on 14 Dec to 09:00 UT on 15 Dec 1999, lagged by 68 min to account for the propagation delay to the ionosphere. The top two panels show solar wind density and velocity data, the middle three panels show IMF data in GSM coordinates, and the bottom two panels show the field magnitude and clock angle.

4 Observations overview: Interval 2 (21:00 UT 14 December – 03:00 UT 15 December 1999)

In this section we now discuss the ground and space observations made during the second of our 6-hour intervals, on 14/15 December 1999.

4.1 Upstream interplanetary conditions

In Fig. 11 we present the ACE interplanetary data in the same format as Fig. 2, lagged by 68 min, for the 18-hour interval from 15:00 UT on 14 December to 09:00 UT on 15 December 1999. The steady nature of the solar wind during the main region of interest is evidenced in the proton number density (n_p) and speed (v_p) data. The density remained

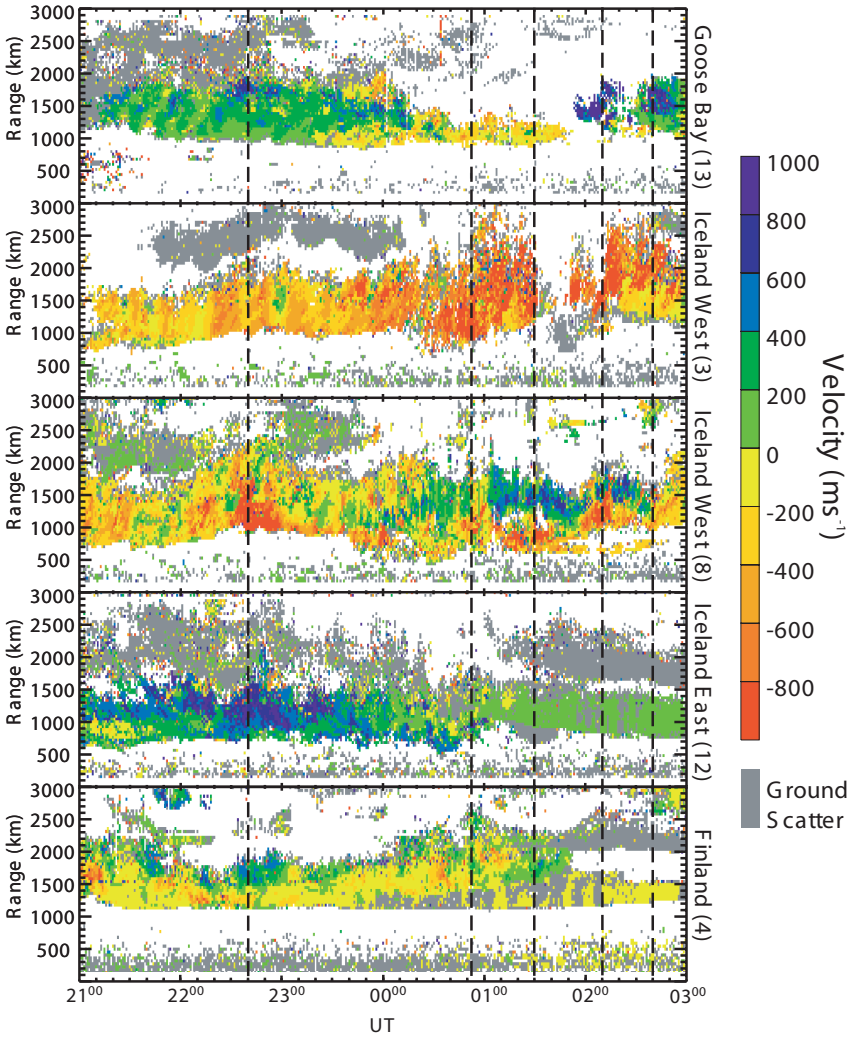

Fig. 12. SuperDARN line-of-sight velocity measurements from the radar beams indicated in Fig. 1a (right side) are shown for the interval 21:00–03:00 UT on 14/15 Dec 1999. The format is the same as Fig. 3.

relatively constant at $\sim 5\,\mathrm{cm}^{-3}$ and the velocity between 370–420 km s^{-1}. The IMF was also steady throughout the main interval. B_x was near zero or negative, B_y was large and negative, and B_z was predominantly positive (and had been for the previous 6 h). This translates to a total field strength of $\sim 8 \pm 2$ nT, and a clock angle with a mean value of $-51°$ and a standard deviation of 15°. However, it may be noted that a small change in the field occurred near the middle of the interval (~00:30 UT), such that the field magnitude and clock angle were modestly increased in the later period compared with the earlier.

4.2 SuperDARN flow data overview

Presented in Fig. 12 are line-of-sight SuperDARN velocity data from the five radar beams, shown by the red lines, in the right-hand map in Fig. 1a. In common with the previous interval, continuous flow was observed over the entire 6 hours, with speeds of ~500–1000 m s^{-1}. These flows are predominantly directed towards the radar at Goose Bay (beam 13) and Iceland East (beam 12), indicative of westward "return" flows in an azimuthally extended dusk convection cell, and away from the radar at Iceland West (beam 3), indicative of sunward "return" flow in the same cell. At Finland (beam 4) for the early part of the interval and Iceland West (beam 8) for the later part, the flows are both towards the radar in the more poleward ranges and away from the radar in the near ranges, indicative of equatorward flow out of the polar cap with a flow reversal in the auroral zone. Again, there is also evidence of strong variability in the flow, which is particularly marked, for example, in the Iceland West data. However, this variability is of a less regular nature than that observed during the previous interval (see Fig. 3). The vertical dashed lines indicate episodes of high flow variability, which will be discussed further in Sect. 4.3 below. To a first approximation, however, this is a similar interval to that discussed above, with dynamic and often high speed flows, driven during an interval of northward and B_y-dominated IMF.

Inspection of data relevant to the identification of sub-

storms (not shown here) also suggests that this is a similar interval to that described above. The H-component magnetometer data again shows only small field variations of a few tens of nT amplitude, indicative of a "quiet" geomagnetic field, similar to that on 2 December shown in Fig. 6. The lack of substorm activity is emphasized in the filtered data, none of which indicates any impulsive substorm-like Pi2 features. Representative data from the LANL97A SOPA instrument (located in the dawn sector, as shown in Fig. 1b) also indicate no injection signatures or indeed any significant variations in the particle fluxes. Overall, therefore, this interval appears to be as devoid of substorm activity as the first. Nevertheless, as mentioned above, impulsive nightside activity was again observed in the flow, which we now go on to examine.

4.3 Nightside flow bursts

In Fig. 13 we present flow parameters extracted from the Map Potential plots as before. The voltage values, again shown in the top panel, lie typically between ∼20 and ∼40 kV. The average over the interval was 29 kV. This is somewhat less than the average during the first interval, possibly due to the slightly reduced IMF magnitude and clock angle. Nevertheless, the values do exhibit a similar variability. The plot of the peak nightside flow speed, however, appears to be divided into two distinct parts. The first half of the interval (up to ∼00:30 UT) appears relatively quiet, with typical values of the peak flow around ∼600–800 m s^{-1} (close to the averaged value of the flow speed over the full 6 h of 732 m s^{-1}). Only one apparent "burst" occurred, at ∼22:40 UT. Then, after ∼00:30 UT, the peak flows resemble more those during the first interval, with regular burst-like features evident in the data, reaching speeds up to ∼1200 m s^{-1}. This change in flow characteristic could be associated with the modest concurrent change in IMF conditions which was noted in Sect. 4.1. Those bursts which can be distinguished from these data (and from a close inspection of the flow maps) have been marked by the vertical dashed lines, corresponding to those in Fig. 12. Comparison with the data in the upper panel of Fig. 13 shows that the peaks which have been identified in the flow speed also generally correspond to peaks in the transpolar voltage. This is consistent with our conclusion about the bursts during the first interval, in that an overall enhancement in the flux transport took place in association with the flow bursts. However, it is also evident that substantial enhancements in the transpolar voltage occurred at times when no flow speed excitation is apparent in the nightside data. This generally occurred early in the interval, when the radar coverage included a significant portion of the dayside ionosphere, and, as can be inferred from the flow maps, the voltage enhancements were then significantly influenced by the dayside driven component of the flow.

The vector components of the peak flow also show a similar trend to the corresponding data from the first interval. The bursts tend to peak in the westward direction (indicated by the solid line), with relatively little enhancement in the north-south component (dashed line). The latitude of the peak flow is generally located in the range 69°–73° (a few degrees lower than observed for the 2 December interval) and does not show significant trends over the interval. This is again consistent with our previous discussion concerning the lack of overall change in the size of the flow pattern. There is some scatter in the local time of the peak flow speed, although around the times of the bursts, specifically in the second half of the interval, the flows did tend to peak consistently within 1–2 h of midnight.

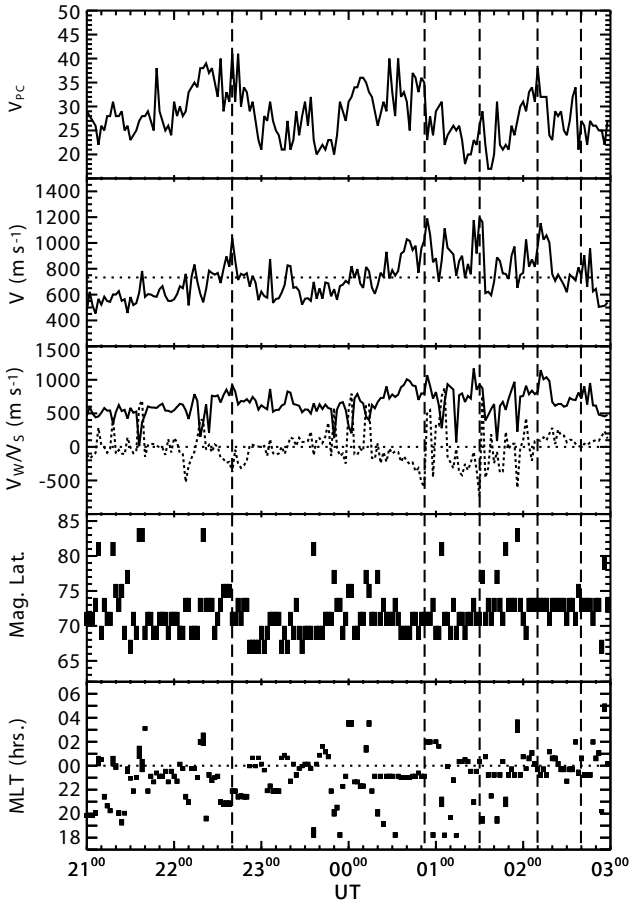

Fig. 13. Flow measurement time series, obtained from the SuperDARN radar observations and "Map-Potential" algorithm for 21:00–03:00 UT on 14/15 Dec 1999. The format is the same as Fig. 7.

4.3.1 Flow burst geometry

As indicated above, the variability of the flows observed here differs somewhat from that observed during the first interval, particularly in the initial period. Although the background flow pattern is similar, being driven under the influence of large negative IMF-B_y, the tail does not seem to respond with quite the same impulsive regularity as before. In Fig. 14a we present four representative examples of the Northern Hemisphere flow pattern, from 21:30 UT on 14 December to 00:30 UT on 15 December, representative of the

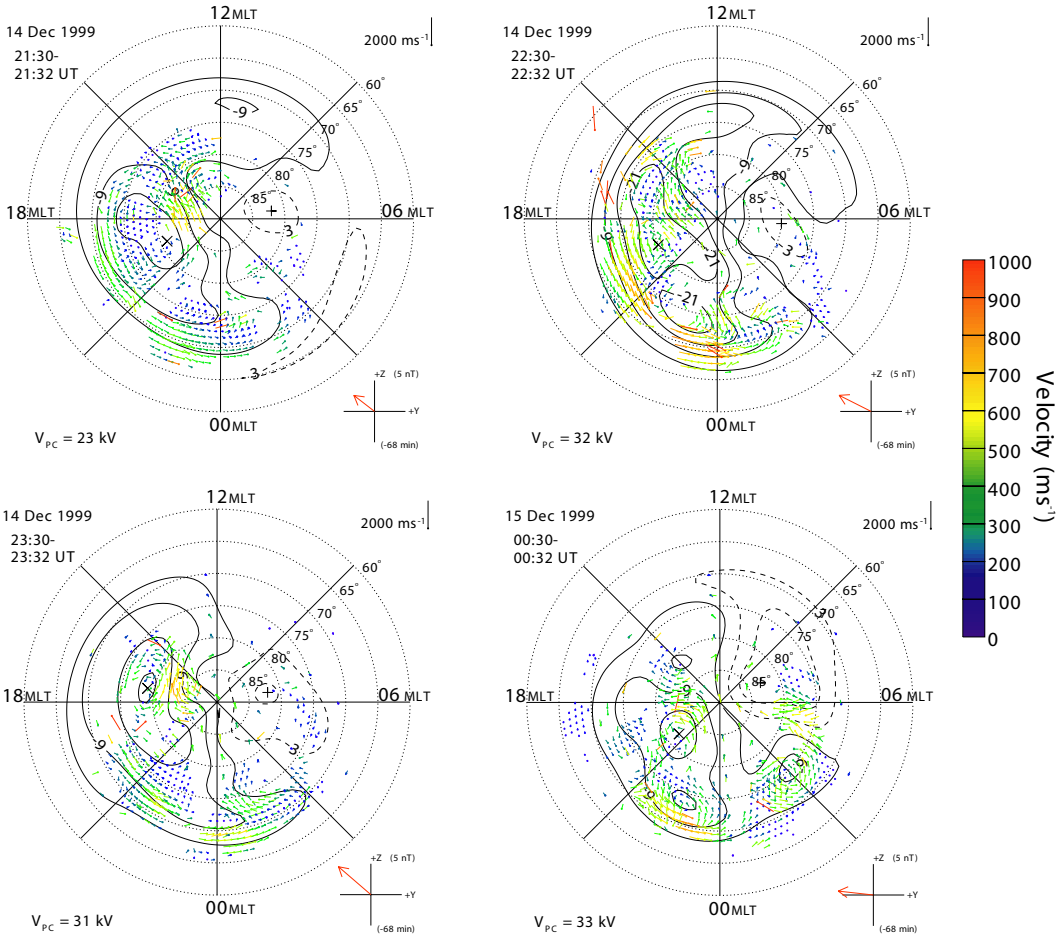

Fig. 14a. SuperDARN flow maps in a similar format to those shown in Fig. 4. Four maps are shown from the 6-h interval for **(a)** the "quiet" half of the interval for which maps are shown on the half hour for 21:30–00:30 UT and **(b)** the 02:10 UT burst from the second half of the interval, spanning 01:54–02:18 UT. The exact time of each 2-min map is indicated in the top left-hand corner. Also indicated on the maps (in b) by the black triangles are the locations of the magnetometer stations colour-coded yellow in Fig. 1b. (Fig. 14 continues).

"quiet" half of the interval, as described above. Although the details vary from plot to plot, the overall flow patterns remain similar to each other, and to that observed during the previous interval (see Fig. 4a). Due to the earlier UT of this interval, however, there is much better coverage of data in the post-noon sector, which shows the existence of dayside anti-sunward flows in the throat of the convection cells, indicative of dayside reconnection. There is also some evidence early on in the interval for the concurrent presence of high-latitude "lobe" convection cells. Later in the interval, in the map at 00:30 UT, for example, a "dawn" flow cell is also apparent, confined essentially to the same dayside MLT quadrant between dawn and noon as in the previous interval. In general, however, the lack of data in the dawn hours makes it difficult to draw conclusions about the nature of the flows in that sector. The extended nature of the dusk flow cell does, nevertheless, imply the existence of the expected dawn-dusk flow asymmetry, which is corroborated by the Southern Hemisphere data (not shown). These data again show much more restricted coverage than in the north, but are consistent with the opposite asymmetry in the flow. Examination of all available DMSP particle data for the interval provides similar corroboration of the open nature of the polar cap. A number of Southern Hemisphere overpasses by the F13 and F14 spacecraft, in particular, provided good evidence of a band of CPS/BPS precipitation at ∼75° (observed at 21, 05, and 09 MLT), with lower energy polar cap precipitation polewards of this.

Although this interval is, therefore, not identical to the first, it is important to point out that some bursts are still observed, particularly in the second half. The centre times of five enhancements in the flow are indicated in Fig. 13 by the vertical dashed lines at 22:40, 00:52, 01:30, 02:10, and 02:40 UT. As mentioned above, the first half of the interval sees only one distinctive burst (the start of which can be seen in the 22:30 UT map of Fig. 14a). In this instance, the burst takes the form of enhanced sunward return flows in the dusk convection cell. During the second half of the interval, when the flow variability was enhanced, the bursts begin to take the form of azimuthal flows in the midnight sector, more like the bursts observed during the first interval. However, they are noticeably less discrete than before, with the flows varying

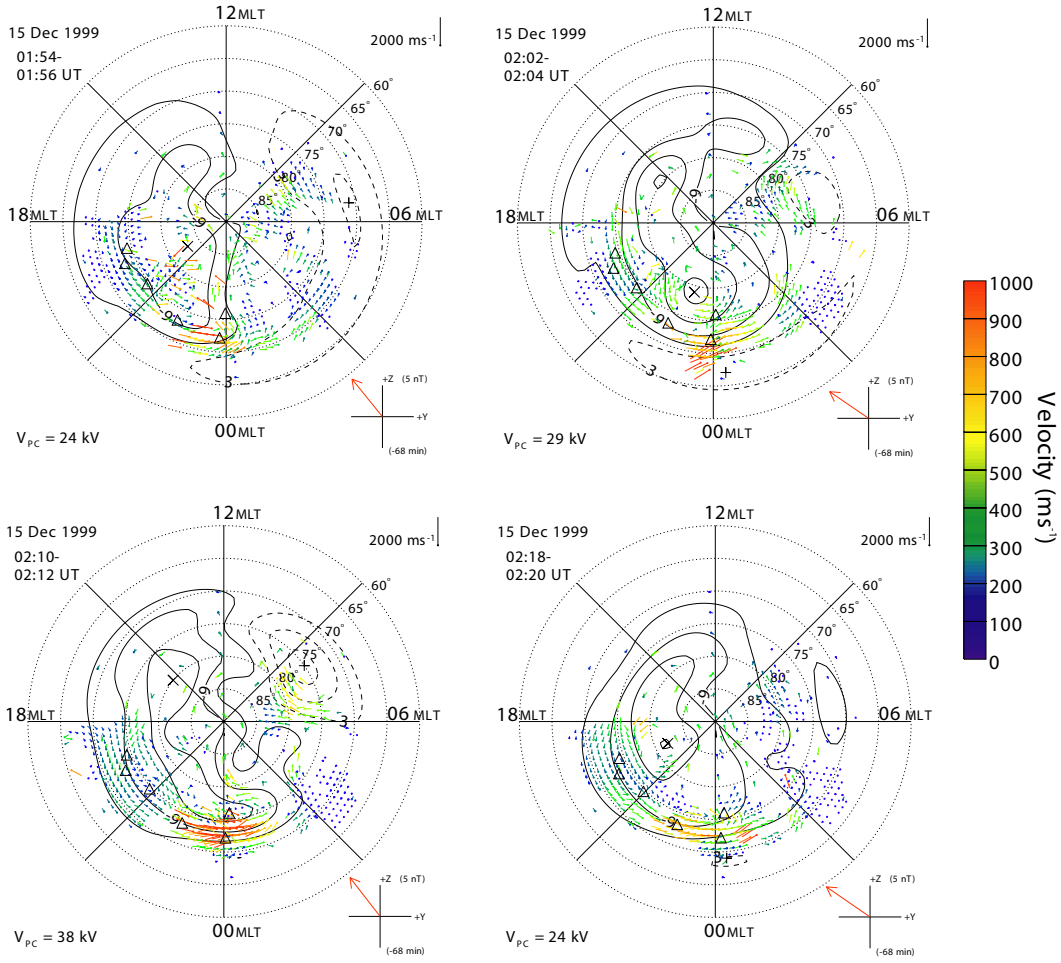

Fig. 14b.

more randomly in magnitude.

The burst centred at ∼02:10 UT is perhaps the best example, and exhibits similar characteristics to the bursts shown in Fig. 8. Therefore, in Fig. 14b we show four flow maps which span this burst between 01:54 and 02:18 UT. The black triangles again show the positions of key ground magnetometer sites whose data will be examined below. The first map, starting at 01:54 UT, is illustrative of the nature of the flow over the ∼20-min period since the end of the previous burst. It shows an IMF B_y-asymmetric flow pattern, with evidence of some enhancement of the westward flow near midnight, and a relatively low transpolar voltage of 24 kV. Over the next ∼20 min, the westward flow in the midnight sector grew in magnitude, peaking at 02:10 UT, with a corresponding peak in transpolar voltage of 38 kV. In the third map, showing this central time of the burst, the flow enhancement consists primarily of westward flows spanning magnetic midnight, similar to a number of the bursts observed during the first interval. Over the following ∼10 min the flows subsided, with the transpolar voltage falling to 24 kV by 02:18 UT.

The main conclusion we wish to draw is that, as in the first interval, continuous quasi-steady Dungey-cycle flow was driven during this 6-h interval of steady interplanetary conditions. This implies again that there must be a consistent nightside reconnection-driven element to the flow which is balancing the observed dayside driving, but which is not manifest as typical substorm phenomena.

4.3.2 Burst magnetic signatures

In Fig. 15 we present magnetometer data for the ∼02:10 UT burst from the high-spatial resolution array shown in the 00:00 UT map in Fig. 1b. Figure 15a presents unfiltered magnetic data along with the corresponding flow components, in the same format as in Fig. 10. Panel (i) contains the H-component magnetic field data (solid line), and the overhead westward component of the flow (dashed line). As found for the bursts during the first interval, there is no consistent correlation between the two data sets. Certain features are present in both, for example, an enhancement in the flow at the location of SKT is accompanied by an increase in the local H-component. In the D-component and the corresponding northward flow (dashed line), shown in panel (ii), there is a similar correlation. Again, however, values of ∼1000 m s^{-1} for the flow speed, and magnetic perturbations of at most ∼50 nT (at these or any of the stations

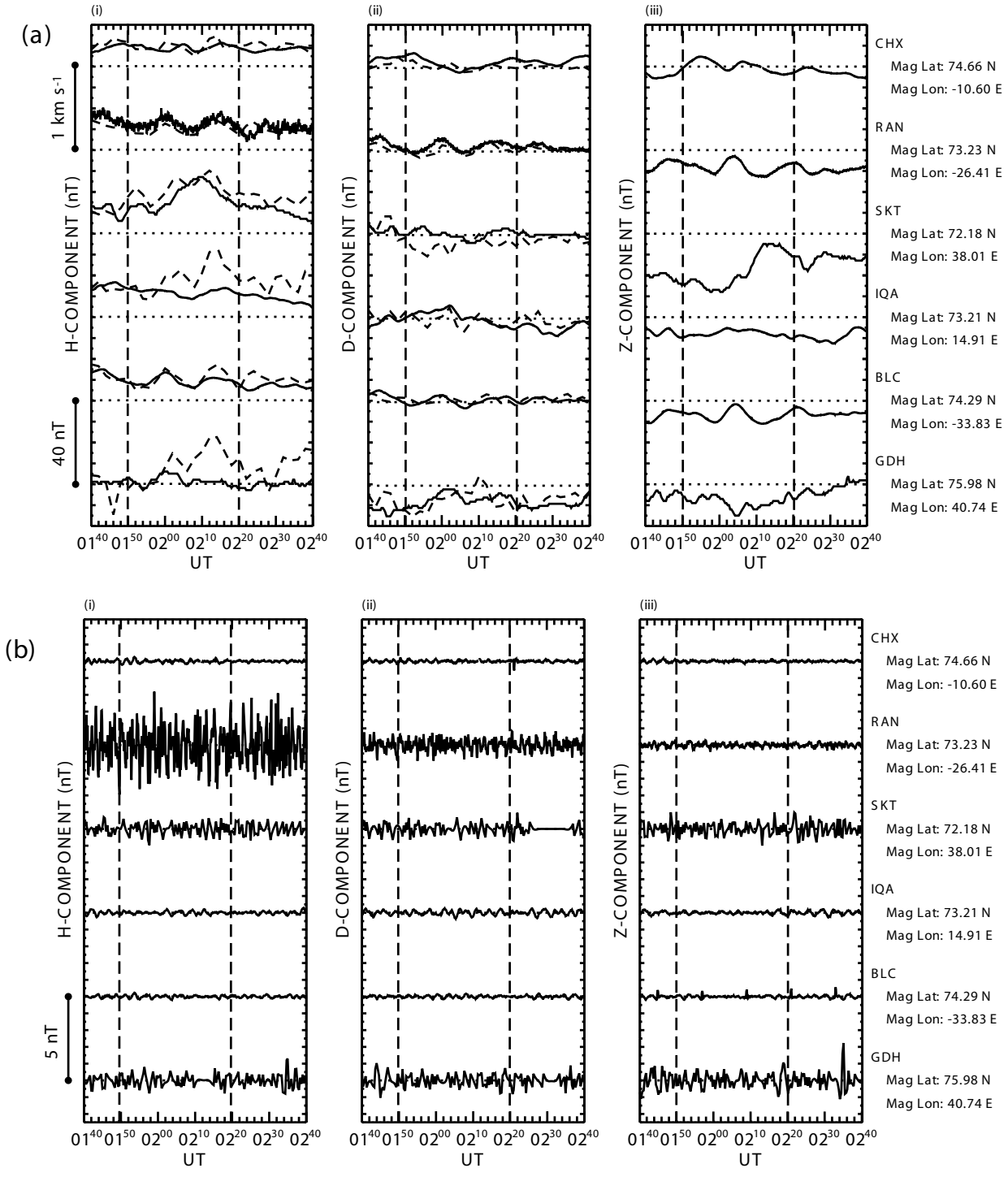

Fig. 15. The H-, D- and Z-components of the ground magnetic field for the interval 01:40–02:40 UT on 14/15 Dec 1999, measured by the stations colour-coded yellow in Fig. 1b, and indicated in Fig. 14b by the black triangles. Also shown are the east-west (in (i)) and north-south (in (ii)) SuperDARN flow components corresponding to the locations of the magnetometers. In **(b)** the magnetic field data has been band-pass filtered (20–200 s) to highlight Pi2-band activity. The scales to the left of each plot indicate the range between the baselines (horizontal dotted lines) and the vertical dashed lines delimit the ∼30 min burst duration.

examined here), imply a Hall conductance of a few mho or less, indicative of a low level of auroral precipitation during these events within the region of enhanced flow.

In Fig. 15b we show the same magnetometer data band-pass filtered between 20–200 s. Station RAN measured the largest amplitude activity in the H- and D-components, but this does not appear to be related to the time of the burst. Indeed, none of the stations show discernable variability in

the Pi2 band over the hour of the plot.

4.4 Interval 2 summary

The second of our two ∼6-h intervals occurred under similar interplanetary conditions to the first. The IMF clock angle remained relatively constant at ∼−50°, somewhat smaller than for the first interval, and the field intensity remained between 6 and 8 nT, also somewhat smaller than before. Dayside reconnection again continued to drive Dungey-cycle flow, although it was observed to be weaker than during the first interval, possibly due to the reduced clock angle and field strength. As before, it was found that the size of the convection pattern remained relatively constant over the entire interval, thus implying that tail reconnection was again ongoing at an average rate approximately equal to that at the dayside. The lack of substorm phenomena was again evidenced in the magnetic and geostationary orbit energetic particle data, while a detailed investigation of the flow data revealed that similar nightside flow bursts occurred. However, only one clear burst was observed during the first half of the interval, with more frequent "bursty" activity occurring during the second half. This change in the nature of the flow coincided with a small change in the IMF conditions, in which the field magnitude was slightly increased and the clock angle slightly reduced. Nevertheless, the basic nature of the bursts appears to be similar to those observed during the first interval.

5 Reconnection rates during burst intervals

The analysis of the principal nightside flow bursts described above shows that the transpolar voltage is enhanced during the bursts, and also suggests (somewhat less strongly) that a modest poleward displacement takes place in the nightside open-closed field line boundary (see Fig. 9). These features indicate that the bursts are associated with enhancements in the nightside reconnection rate. In this section we analyse these data further, and attempt to quantify the reconnection rates within the limitations of the information available. The theoretical framework of our discussion is the Cowley and Lockwood (1992) paradigm of reconnection-associated flow excitation, leading to the reconnection-rate formulas derived previously by Grocott et al. (2002).

The physical situation which applies here is shown in Fig. 16 (where for simplicity the B_y-associated asymmetry is not represented), in which we assume that dayside and nightside reconnection are both continuously present, but that the rate of flux closure on the nightside exceeds that on the dayside, such that overall, the polar cap contracts. In this diagram the segments of the open-closed field line boundary mapping to the reconnection sites (i.e. the "merging gaps") are shown by the dot-dashed lines, while the adiaroic segments of the boundary (which are not so connected and which thus move with the flow) are shown by the heavy solid lines. The lighter arrowed lines show the plasma streamlines.

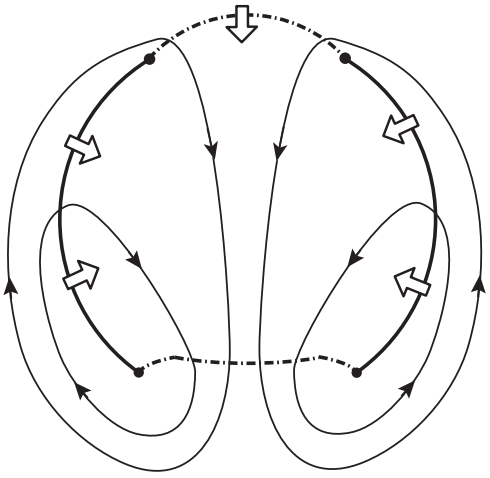

Fig. 16. Schematic of the flow situation appropriate to the burst intervals examined here, in which dayside and nightside reconnection are both continuously present, but with the rate of flux closure on the nightside exceeding the rate of open flux creation at the dayside, such that overall the polar cap contracts. The segments of the open-closed field line boundary mapping to the reconnection sites (i.e. the "merging gaps") are shown by the dot-dashed lines, while the adiaroic segments of the boundary (which are not so connected and which thus move with the flow) are shown by the heavy solid lines. The lighter arrowed lines again show the plasma streamlines, and the large arrows show the implied boundary motion.

The action of the flow is to transport closed flux from the merging gap region of closure sunward to other local times, such as (in effect) to distribute the newly-closed flux around the boundary. In the Cowley-Lockwood paradigm the flux is distributed uniformly round the boundary, such that it contracts with its shape unchanged. A key feature of the diagram is that the foci of the plasma flow cells under these circumstances will be located near the ends of the nightside merging gap (see also, e.g. Siscoe and Huang, 1985). At these points the plasma flow across the boundary will reverse from being directed equatorward in the sector of the merging gap, to being poleward in the contracting adiaroic sector on either side. Thus, we expect in this case that the total transpolar voltage (as estimated from the SuperDARN radar data) will correspond to the ionospheric voltage across the nightside merging gap. By the same argument, when dayside reconnection dominates, the transpolar voltage will correspond instead to the ionospheric voltage across the dayside merging gap. These conclusions would not follow if, for example, significant voltages are also present associated with "lobe" convection cells. However, as indicated above, we have not found evidence for a substantial contribution from such flows cells in the data examined here.

Under these conditions, Grocott et al. (2002) have shown that the nightside and dayside reconnection rates averaged over some interval τ, $\langle\dot{\Phi}_n\rangle$ and $\langle\dot{\Phi}_d\rangle$, respectively, can be estimated from

$$\langle\dot{\Phi}_n\rangle \approx -\langle V_{PC}\rangle + f_{mg}\frac{B_i\,\Delta A}{\tau} \quad \text{and} \tag{1a}$$

$$\langle \dot{\Phi}_d \rangle = \langle V_{PC} \rangle + \left(1 - f_{mg}\right) \frac{B_i \, \Delta A}{\tau} \,. \quad (1b)$$

Here the reconnection rates are represented in terms of the rates of change of the amount of open flux Φ, such that by definition, $\langle \dot{\Phi}_n \rangle$ is negative while $\langle \dot{\Phi}_d \rangle$ is positive. In these equations $\langle V_{PC} \rangle$ is the averaged polar cap voltage, as obtained from the SuperDARN data (assumed equal to the voltage across the nightside merging gap, as indicated above), B_i is the polar magnetic field strength (taken to be constant for simplicity and equal to 60 000 nT), ΔA is the change in the area of open flux over the interval (negative for a contraction), and f_{mg} is the fraction of that area associated with the motion of the nightside merging gap. If the contraction is uniform, as assumed in the Cowley-Lockwood paradigm, then f_{mg} is also equal to the fraction of the total length of the open-closed field line boundary occupied by the nightside merging gap.

Examining Eq. (1) we can see that if $\Delta A \approx 0$ for a particular interval (as is true overall for the intervals considered here), then the magnitudes of the mean dayside and nightside reconnection rates are both equal to the mean polar cap voltage $\langle V_{PC} \rangle$. On the other hand, if the polar cap area contracts during the interval, such that $\Delta A < 0$, then the magnitude of the nightside reconnection rate will be greater than $\langle V_{PC} \rangle$, while that of the dayside reconnection rate will be less than $\langle V_{PC} \rangle$. An inconsistency occurs if the magnitude of the second term in Eq. (1b) exceeds the first, implying that $\langle \dot{\Phi}_d \rangle$ is negative, contrary to assumption. If this is found to be the case, the implication is that the closed flux is not distributed uniformly around the boundary by the flow as assumed. However, for the events analysed here, a more stringent condition on $\langle \dot{\Phi}_d \rangle$ may be considered, since we have argued in the present case that, over the interval as a whole the dayside and nightside reconnection rates must be in approximate balance. Thus, in the absence of an unlikely anti-correlation between the dayside and nightside reconnection rates, the value of $\langle \dot{\Phi}_d \rangle$ during the nightside burst events should not generally differ greatly from the polar cap voltage averaged over the whole interval. For the first 6-h interval considered here (on 2 December), the transpolar voltage averaged over the whole interval determined from the SuperDARN data was ~35 kV, while for the second (on 14/15 December) it was ~28 kV (see Figs. 7 and 13).

We now use Eqs. (1a) and (1b) to estimate the reconnection rates during the first burst interval. As discussed in Sect. 3.4.2, this is the only burst of the three studied in detail here in which the radar data clearly define the flow reversal boundary. If we examine these equations, it is clear that some of the parameters on the right-hand sides are determined by the data better than others. In particular, the mean polar cap voltage $\langle V_{PC} \rangle$ during the burst is reasonably well determined from the SuperDARN data, while the net area swept out by the open-closed field line boundary ΔA and the fraction f_{mg} of that associated with the nightside merging gap are not so well determined. With regard to f_{mg}, values can be estimated by inspection of the flow patterns during the burst interval. We have argued above that the maximum and minimum in the electric potential lie at either end of the nightside merging gap, under the nightside "burst" conditions investigated here. Identification of the location of the foci of the flow cells provides, therefore, an indication of the magnetic local time extent of the merging gap, from which f_{mg} can be estimated. However, with regard to the change in polar cap area, we have been able to make only an approximate determination of the poleward displacement of the boundary, quantized in 1° latitude steps, in one nightside local time sector, where a clearly defined flow reversal is evident. As in the study by Grocott et al. (2002), our approach has been, therefore, to look at the sensitivity of the results to these less-well determined parameters.

What we have done (in effect) is to plot a contour map of $\langle \dot{\Phi}_n \rangle$ and $\langle \dot{\Phi}_d \rangle$ on the $f_{mg} - \Delta A$ plane, and to delineate regions of consistency both with the rather roughly obtained limits on these latter parameters, and on $\langle \dot{\Phi}_d \rangle$, as discussed above. However, rather than use ΔA directly, we have used instead the latitude displacement of the boundary in the local time sector in which this has been determined via the analysis presented above (in Fig. 9). From this displacement the areas ΔA have been calculated by extrapolation of the initial and final boundary positions to other local times. Specifically, we have assumed for simplicity (and in accordance with the Cowley-Lockwood paradigm) that the initial and final boundaries are circles drawn about a common centre. The chosen centre is displaced from the magnetic pole by 2° of magnetic latitude towards the nightside, this also being the chosen "centre" of the spherical harmonic analysis of the SuperDARN data. Examination of the flow patterns overall indicates that this is a very reasonable choice, and that no substantial improvement would result from attempting to use some more complicated boundary shape.

Our results for the burst occurring during 02:46–03:15 UT on 2 December are shown in Fig. 17, based on the data shown in Fig. 9. Here reconnection rate contours are plotted on the $f_{mg} - \Delta\Lambda_B$ plane, where f_{mg} is shown on the vertical axis, and the displacement of the magnetic latitude of the flow reversal boundary $\Delta\Lambda_B$ during the event is shown on the horizontal axis. From the latter parameter we have then calculated the change in area of the polar cap according to the above algorithm, starting from an initial boundary position at $\Lambda_B = 76°$ in this case (Fig. 9), so that ΔA becomes increasingly negative as we move from left to right across the plot. For this event we find that a 1° poleward displacement of the boundary in the 21:00 MLT sector corresponds to a flux closure of $B_i \Delta A \approx -0.6 \times 10^8$ Wb, while 2° corresponds to -1.1×10^8 Wb and 3° to -1.5×10^8 Wb. Using a value of the averaged transpolar voltage of $\langle V_{PC} \rangle = 42$ kV for the interval, determined from the data shown in Fig. 9, we have then plotted contours of $\langle \dot{\Phi}_n \rangle$ and $\langle \dot{\Phi}_d \rangle$, shown by the solid and dashed lines, respectively. At the left-hand edge of the plot we have $\Delta\Lambda_B = 0$ (and $\Delta A = 0$), so that at this limit Eqs. (1a) and (1b) give $\langle \dot{\Phi}_d \rangle = -\langle \dot{\Phi}_n \rangle = \langle V_{PC} \rangle$, as discussed above. We also have $\langle \dot{\Phi}_n \rangle = -\langle V_{PC} \rangle$ along the bottom edge of the plot, where $f_{mg} = 0$, and $\langle \dot{\Phi}_d \rangle = \langle V_{PC} \rangle$ along the top edge of the plot, where $f_{mg} = 1$. Away from these respec-

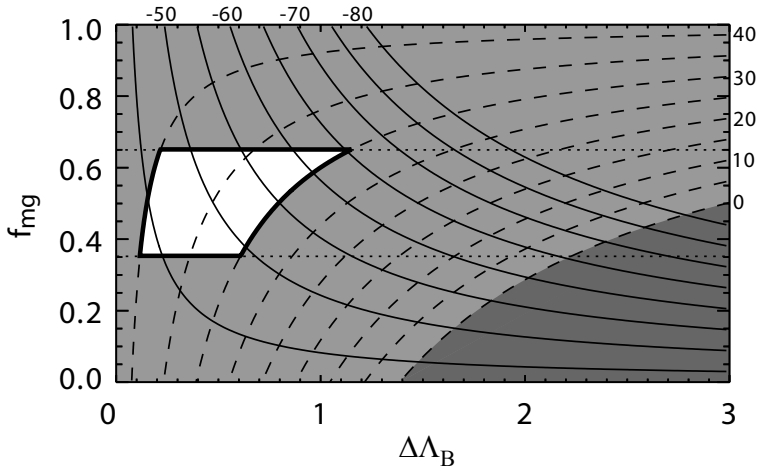

Fig. 17. Reconnection rate contours plotted on the $f_{mg} - \Delta\Lambda_B$ plane, where the fraction of the open-closed field line boundary occupied by the nightside merging gap, f_{mg}, is shown on the vertical axis, and the poleward displacement of the magnetic latitude of the nightside flow reversal boundary $\Delta\Lambda_B$ during the event is shown on the horizontal axis. The dark-shaded area in the bottom right corner of each plot represents an area of inconsistent results where the dayside reconnection rate becomes negative. The horizontal dotted lines mark the likely range of f_{mg} for the event (obtained from the SuperDARN maps), with the exterior region shown shaded. Also shaded is the region of unreasonable dayside reconnection rates as discussed in the text. The remaining unshaded area corresponds to the region of solutions that conforms to all of these constraints. These results are plotted for the 03:00 UT burst on 2 Dec.

tive boundaries, $\langle\dot{\Phi}_n\rangle$ becomes increasingly negative as f_{mg} and $\Delta\Lambda_B$ both increase, while $\langle\dot{\Phi}_d\rangle$ drops to smaller values as f_{mg} decreases and $\Delta\Lambda_B$ increases. Eventually, $\langle\dot{\Phi}_d\rangle$ becomes negative in the dark-shaded area in the bottom right corner of the plot, this representing an area of inconsistent results (as discussed above) when $(1 - f_{mg}\ \Delta A$ becomes too negative.

We now consider the likely ranges of the controlling parameters, and the consequent likely range of values of the reconnection rates. First, examination of the flow maps during the interval indicates that the nightside merging line is relatively extended, with f_{mg} lying in the range ∼0.35 to 0.65, corresponding to 0.15 on either side of the average value for the duration of the burst. This range is marked by the horizontal dotted lines, with the exterior region shown as shaded. Second, according to the above argument, we can reasonably expect the dayside reconnection rate to have fallen in the range ∼30 to ∼40 kV, corresponding to 5 kV on either side of the total transpolar voltage, averaged over the whole 6-h interval of observations. The region outside these limits is also shaded. The remaining unshaded area then represents the solutions which are compatible with both of these constraints. The location of this area first suggests an overall poleward boundary displacement between ∼0.5° and ∼1°, reasonably consistent with the ∼1° displacement inferred in Fig. 9. It also suggests nightside reconnection rates of ∼45–60 kV, which thus exceed concurrent dayside rates by 10–20 kV.

The implication of these results is that during the burst interval examined here, the nightside reconnection rate exceeded the dayside reconnection rate by 50%. Under conditions of weak northward-directed, but B_y-dominated IMF, therefore, it appears that the flow continues to be dominated by Dungey-cycle flow, as it is during intervals of southward-directed IMF, and the "return" flow from the tail is often bursty and sporadic. However, our data also show that these bursts are not accompanied by phenomena characteristic of substorms, such as enhanced auroral zone conductivities, magnetic bays, Pi2s, or geostationary energetic particle injections. It seems likely that the impulsive phenomena concerned, while possibly being related physically to substorms, were taking place considerably further down the tail than is typical of more strongly-driven intervals.

6 Summary and conclusions

We have discussed the ionospheric flow and magnetic disturbance which occurred during two 6-h near-steady intervals of northward, but B_y-dominated IMF. During the first interval, on 2 December 1999, the average IMF clock angle was ∼−60° and the field strength was ∼10 nT. During the second interval, on 14/15 December 1999, the average IMF clock angle was ∼−50°, and the field strength was ∼7 nT. Both sets of conditions gave rise to similar continuous flows in the polar ionosphere, with a highly asymmetric twin-vortex pattern being observed, consistent with directly driven Dungey-cycle convection. This flow was slightly weaker during the second interval compared with the first (the mean transpolar voltage was 29 kV compared to 35 kV), possibly due to the reduced IMF clock angle and field strength. On shorter time scales, however, the flow exhibited intervals of strong variability in the nightside ionosphere, which differed slightly in nature between the two intervals. During the 2 December interval, ∼1000 m s^{-1} bursts of flow were observed in the mid-

night sector, lasting a few tens of minutes and recurring every hour or so. They were accompanied by weak magnetic signatures (∼10 nT) and low amplitude Pi2-band (5–50 mHz) activity, although it is not clear that either were directly associated. During the 14/15 December interval, the bursts were observed to be less regular, with only one discernable event occurring during the first half of the interval. During the second half, the bursts become more frequent, but appear to be less distinct from one another than those observed during the first interval.

Over the entire 6 h of each interval, it was observed that the size of the convection pattern remained relatively constant. This implies that tail reconnection was ongoing, at an average rate approximately equal to that at the dayside magnetopause. However, the nightside flow observations then indicate that this reconnection typically was not steady, but underwent sporadic enhancements, giving rise to the flow burst intervals. This is indicated by the fact that each burst was accompanied by an enhancement in the total transpolar voltage, and in one example, where the flow reversal boundary was well observed, appeared to be coincident with a small (∼1°) contraction of the polar cap boundary. These bursts are, therefore, likely to be an ionospheric manifestation of convective transport away from a distant tail reconnection site. A simple model of this process, based on the Cowley and Lockwood (1992) picture of reconnection-associated flow excitation, has enabled us to make an estimate of the nightside reconnection rate associated with one of these burst intervals, based on assumed limits on the dayside rate. We estimate that, during this burst, the nightside reconnection rate was elevated typically to values ∼45–60 kV, thus exceeding the likely concurrent dayside reconnection rates of ∼30–40 kV by 50%. Bearing in mind the fact that over the full 6 h of each interval, the polar cap remains relatively constant in size, this also implies a "non-burst" nightside reconnection rate of ∼20–25 kV. While not manifest as substorms, these discrete bursts of enhanced tail reconnection seem clearly to be a related phenomenon occurring, as suggested above, much further down-tail. In effect, we have demonstrated that while under conditions of southward IMF, the Dungey cycle will usually be manifest as the substorm cycle; the two are not, in fact, synonymous. Intermediate interplanetary conditions exist, such as those considered here, in which the Dungey cycle continues to drive the system, but without evidence of classic substorms being observed (though tail activity appears still to be pulsed on ∼1-h time scales). The question remains as to exactly what range of interplanetary conditions gives rise to a tail response of this nature. We also need to investigate the corresponding picture for positive B_y-dominated IMF. These questions, however, remain the subject of future work.

Acknowledgements. We would like to thank the PIs of the SuperDARN radars for provision of the radar data employed in this study. The data employed were from radars funded by the research funding agencies of Canada, France, the UK, USA, Japan, and Australia. We would also like to thank Dr. Mike Ruohoniemi of the Johns Hopkins University Applied Physics Laboratory for provision of the "Map-Potential" algorithm software. For the ground magnetometer data, we thank the Finnish Meteorological Institute and its co-institutes who maintain the IMAGE magnetometer array, the Canadian Space Agency who constructed and maintain the CANOPUS instrument array, the Geological Survey of Canada (Natural Resources Canada) for use of data from its magnetometer array, Boston University and Augsburg College who run the MACCS magnetometer array (supported by the National Science Foundation), Jurgen Watermann and the Danish Meteorological Institute for the Greenland data, and Ian Mann and David Milling for the SAMNET data. SAMNET is a PPARC National Facility deployed and operated by the University of York. The DMSP particle detectors were designed by Dave Hardy of AFRL, and data were obtained from JHU/APL. We thank Dave Hardy, Fred Rich, and Patrick Newell for its use. We would also like to thank Geoff Reeves and the Los Alamos National Laboratory for LANL particle data, Norman Ness and Charles Smith for provision of ACE magnetometer data, David McComas for provision of ACE SWEPAM data and Louis Frank for the use of the Geotail data. AG was supported during this study by a PPARC Quota Studentship, and SWHC by PPARC Senior Fellowship PPA/N/S/2000/00197. SuperDARN studies and operations at the University of Leicester are supported by PPARC grants PPA/G/O/1999/00181 and PPA/R/R/1997/00256 respectively.

The Editor in chief thanks R. L. Lyons and A. D. M. Walker for their help in evaluating this paper.

References

Angelopoulos, V., Baumjohann, W., Kennel, C. F., Coroniti, F. V., Kivelson, M. G., Pellat, R., Walker, R. J., Lühr, H., and Paschmann, G.: Bursty bulk flows in the central plasma sheet, J. Geophys. Res., 97, 4027–4039, 1992.

Baker, D. N., Pulkkinen, T. I., Angelopoulos, V., Baumjohann, W., and McPherron, R. L.: Neutral line model of substorms: Past results and present view, J. Geophys. Res., 101, 12 975–13 010, 1996.

Baker, K. B. and Wing, S.: A new magnetic coordinate system for conjugate studies at high latitudes, J. Geophys. Res., 94, 9139–9143, 1989.

Baumjohann, W., Paschmann, G., and Lühr, H.: Characteristics of high-speed flows in the plasma sheet, J. Geophys. Res., 95, 3801–3809, 1990.

Belian, R. D., Gisler, G. R., Cayton, T., and Christensen, R.: High-Z energetic particles at geostationary orbit during the great solar proton event series of October 1989, J. Geophys. Res., 97, 16 897–16 906, 1992.

Bristow, W. A., Ruohoniemi, J. M., and Greenwald, R. A.: Super Dual Auroral Radar Network observations of convection during a period of small-magnitude northward IMF, J. Geophys. Res, 103, 4051–4061, 1998.

Cowley, S. W. H.: Magnetospheric asymmetries associated with the Y-component of the IMF, Planet. Space Sci., 29, 79–96, 1981.

Cowley, S. W. H. and Lockwood, M.: Excitation and decay of solar wind-driven flows in the magnetosphere-ionosphere system, Ann. Geophysicae, 10, 103–115, 1992.

de la Beaujardière, O., Lyons, L. R., Ruohoniemi, J. M., Friis-Christensen, E., Danielsen, C., Rich, F. J., and Newell, P. T.: Quiet-time intensifications along the poleward boundary near midnight, J. Geophys. Res., 99, 287–298, 1994.

Dungey, J. W.: Interplanetary magnetic field and the auroral zones, Phys. Rev. Lett., 6, 47–48, 1961.

Dungey, J. W.: The structure of the exosphere, or, adventures in velocity space, Geophysics, in: The Earth's Environment, (Eds) Dewitt, C., Hieblot, J., and Lebau, A., Gordon and Breach, Newark, N.J., p505, 1963.

Elphic, R. C., Lockwood, M., Cowley, S. W. H., and Sandholt, P. E.: Flux transfer events at the magnetopause and in the ionosphere, Geophys. Res. Lett., 17, 2241–2244, 1990.

Etemadi, A., Cowley, S. W. H., Lockwood, M., Bromage, B. J. I., Willis, D. M., and Lühr, H.: The dependence of high-latitude dayside ionospheric flows on the north-south component of the IMF: a high-time resolution correlation analysis using EISCAT "Polar" and AMPTE UKS and IRM data, Planet. Space Sci., 36, 471–498, 1988.

Fairfield, D. H. and Cahill, L. J., Jr.: Transition region magnetic field and polar magnetic disturbances, J. Geophys. Res., 71, 155–167, 1966.

Farrugia, C. J., Freeman, M. P., Burlaga, L. F., Lepping, R. P., and Takahashi, K.: The Earth's magnetosphere under continued forcing: Substorm activity during the passage of an interplanetary magnetic cloud, J. Geophys. Res., 98, 7657–7671, 1993.

Frank, L. A., Ackerson, K. L., Paterson, W. R., Lee, J. A., English, M. R., and Pickett, G. L.: The comprehensive plasma instrumentation (CPI) for the Geotail spacecraft, J. Geomag. and Geoelec., 46, 23–31, 1994.

Frank, L. A., Sigwarth, J. B., Craven, J. D., Cravens, J. P., Dolan, J. S., Dvorsky, M. R., Hardebeck, P. K., Harvey, J. D., and Muller, D. W.: The Visible Imaging System (VIS) for the Polar spacecraft, Space Sci. Rev., 71, 297–311, 1995.

Friis-Christensen, E., Kamide, Y., Richmond, A. D., and Matsushita, S.: Interplanetary magnetic field control of high-latitude electric fields and currents determined from Greenland magnetometer data, J. Geophys. Res., 90, 1325–1338, 1985.

Gjerloev, J. W. and Hoffman, R. A.: The convection electric field during auroral substorms, J. Geophys. Res, 106, 12 919–12 931, 2001.

Grant, I. F., McDiarmid, D. R., and McNamara, A. G.: A class of high-m pulsations and its auroral radar signature, J. Geophys. Res., 97, 8439–8451, 1992.

Greenwald, R. A., Baker, K. B., Dudeney, J. R., Pinnock, M., Jones, T. B., Thomas, E. C., Villain, J.-P., Cerisier, J.-C., Senior, C., Hanuise, C. , Hunsucker, R. D., Sofko, G., Koehler, J., Nielsen, E., Pellinen, R., Walker, A. D. M., Sato, N., and Yamagishi, H.: DARN/SuperDARN: A global view of the dynamics of high-latitude convection, Space Sci. Rev., 71, 761–796, 1995.

Grocott, A., Cowley, S. W. H., Sigwarth, J. B., Watermann, J. F., and Yeoman, T. K.: Excitation of twin-vortex flow in the nightside high-latitude ionosphere during an isolated substorm, Ann. Geophysicae, 20, 1577–1601, 2002.

Hardy, D. A., Schmitt, L. K., Gussenhoven, M. S., Marshall, F. J., Yeh, H. C., Shumaker, T. L., Hube, A., and Pantazis, J.: Precipitating electron and ion detectors (SSJ/4) for the block 5D/Flights 6-10 DMSP satellites: Calibration and data presentation, Rep. AFGL-TR-84-0317, Air Force Geophys. Lab., Hanscom Air Force Base, Mass., 1994.

Henderson, M. G., Reeves, G. D., and Murphree, J. S.: Are north-south aligned auroral structures an ionospheric manifestation of bursty bulk flows?, Geophys. Res. Lett., 25, 3737–3740, 1998.

Heppner, J. P. and Maynard, N. C.: Empirical high-latitude electric field models, J. Geophys. Res., 92, 4467–4489, 1987.

Hones, Jr., E. W.: Transient phenomena in the magnetotail and their relation to substorms, Space Sci. Rev., 23, 393–410, 1979.

Huang, C.-S., Sofko, G. J., Koustov, A. V., MacDougall, J. W., Greenwald, R. A., Ruohoniemi, J. M., Villain, J. P., Lester, M., Watermann, J., Papitashvili, V. O., and Hughes, W. J.: Long-period magnetospheric-ionospheric perturbations during northward interplanetary magnetic field, J. Geophys. Res., 106, 13 091–13 103, 2001.

Hughes, W. J. and Engebretson, M. J.: MACCS: Magnetometer Array for Cusp and Cleft Studies, in: Satellite-Ground Based Coordination Sourcebook, (Eds) Lockwood, M., Wild, M. N., and Opgenoorth, H. J., ESA-SP-1198, 119–127, 1997.

Jørgensen, T. S., Friis-Christensen, E., and Wilhjelm, J.: Interplanetary magnetic fields and high-latitude ionospheric currents, J. Geophys. Res., 77, 1976–1977, 1972.

Kirkwood, S., Opgenoorth, H. J., and Murphree, J. S.: Ionospheric conductivities, electric fields and currents associated with auroral substorms measured by the EISCAT radar, Planet. Space Sci., 36, 1359–1380, 1988.

Khan, H. and Cowley, S. W. H.: Observations of the response time of high latitude ionospheric convection to variations in the interplanetary magnetic field using EISCAT and IMP-8 data, Ann. Geophysicae, 17, 1306–1335, 1999.

Khan, H., Cowley, S. W. H., Kolesnikova, E., Lester, M., Brittnacher, M. J., Hughes, T. J., Hughes, W. J., Kurth, W. S., McComas, D. J., Newitt, L., Owen, C. J., Reeves, G. D., Singer, H. J., Smith, C. W., Southwood, D. J., and Watermann, J. F.: Observations of two complete substorm cycles during the Cassini Earth swingby: Cassini magnetometer data in a global context, J. Geophys. Res., 106, 13 141–13 175, 2001.

Lockwood, M., Sandholt, P. E., Cowley, S. W. H., and Oguti, T.: Interplanetary field control of dayside auroral activity and the transfer of momentum across the dayside magnetopause, Planet. Space Sci., 37, 1347–1365, 1989.

Lühr, H., Aylward, A., Bucher, S. C., Pajunpaa, A., Pajunpaa, K., Holmboe, T., and Zalewski, S. M.: Westward moving dynamic substorm features observed with the IMAGE magnetometer network and other ground-based instruments, Ann. Geophysicae, 16, 425–440, 1998.

Lyons, L. R., Nagai, T., Blanchard, G. T., Samson, J. C., Yamamoto, T., Mukai, T., Nishida, A., and Kokubun, S.: Association between Geotail plasma flows and auroral poleward boundary intensifications observed by CANOPUS photometers, J. Geophys. Res., 104, 4485–4500, 1999.

Machida, S., Miyashita, Y., Ieda, A., Nishida, A., Mukai, T., Saito, Y., and Kokubun, S.: Geotail observations of flow velocity and north-south magnetic field variations in the near and mid-distant tail associated with substorm onsets, Geophys. Res. Lett., 26, 635–638, 1999.

McComas, D. J., Bame, S. J., Barker, P., Feldman, W. C., Phillips, J. L., Riley, P., and Griffee, J. W.: Solar Wind Electron Proton Alpha Monitor (SWEPAM) for the Advanced Composition Explorer, Space Sci. Rev., 86, 563–612, 1998.

Milan, S. E., Lester, M., Cowley, S. W. H., and Brittnacher, M.: Convection and auroral response to a southward turning of the IMF: Polar UVI, CUTLASS, and IMAGE signatures of transient magnetic flux transfer at the magnetopause, J. Geophys. Res., 105, 15 741–15 755, 2000.

Morelli, J. P., Bunting, R. J., Cowley, S. W. H., Farrugia, C. J., Freeman, M. P., Friis-Christensen, E., Jones, G. O .L., Lester, M., Lewis, R. V., Lühr, H., Orr, D., Pinnock, M., Reeves, G. D., Williams, P. J. S., and Yeoman, T. K.: Radar observations of auroral zone flows during a multiple-onset substorm, Ann. Geophysicae, 13, 1144–1163, 1995.

Nagai, T., Fujimoto, M., Saito, Y., Machida, S., Teresawa, T., Naka-

mura, R., Yamamoto, T., Mukai, T., Nishida, A., and Kokubun, S.: Structure and dynamics of magnetic reconnection for substorm onsets with Geotail observations, J. Geophys. Res., 103, 4419–4440, 1998.

Newell, P. T., Burke, W. J., Sanchez, E. R., Meng, C.-I., Greenspan, M. E., and Clauer, C. R.: The low-latitude boundary layer and the boundary plasma sheet at low altitude: Prenoon precipitation regions and convection reversal boundaries, J. Geophys. Res., 96, 21 013–21 023, 1991.

Newell, P. T., Feldstein, Y. I., Galperin, Y. I., and Meng, C.-I.: Morphology of nightside precipitation, J. Geophys. Res., 101, 10 737–10 748, 1996.

Neudegg, D. A., Yeoman, T. K., Cowley, S. W. H., Provan, G., Haerendel, G., Baumjohann, W., Auster, U., Fornaçon, K.-H., Georgescu, E., and Owen, C. J.: A flux transfer event observed at the magnetopause by the Equator-S spacecraft and in the ionosphere by the CUTLASS HF radar, Ann. Geophysicae, 17, 707–711, 1999.

Opgenoorth, H. J. and Pellinen, R. J.: The reaction of the global convection electrojets to the onset and expansion of the substorm current wedge, in: "Substorms-4", (Eds) Kokobun, S. and Kamide, Y., Terra Sci. Publ. Co., Tokyo, 663–668, 1998.

Petrukovich, A. A., Sergeev, V. A., Zleneyi, L. M., Mukai, T., Yamamoto, T., Kokubun, S., Shiokawa, K., Deehr, C. S., Budnick, E. Y., Büchner, J., Fedorov, A. O., Grigorieva, V. P., Hughes, T. J., Pissarenko, N. F., Romanov, S. A., and Sandahl, I.: Two spacecraft observations of a reconnection pulse during an auroral breakup, J. Geophys. Res., 103, 47–59, 1998.

Pinnock, M., Rodger, A. S., Dudeney, J. R., Baker, K. B., Greenwald, R. A., and Greenspan, M.: Observations of an enhanced convection channel in the cusp ionosphere, J. Geophys. Res., 98, 3767–3776, 1993.

Provan, G., Yeoman, T. K., and Milan, S. E.: CUTLASS Finland radar observations of the ionospheric signatures of flux transfer events and the resulting plasma flows, Ann. Geophysicae, 16, 1411–1422, 1998.

Reiff, P. H. and Burch, J. L.: IMF B_y-dependent plasma flow and Birkland currents in the dayside magnetosphere 2. A global model for northward and southward IMF, J. Geophys. Res., 90, 1595–1609, 1985.

Reiff, P. H., Spiro, R. W., and Hill, T. W.: Dependence of polar cap potential drop on interplanetary parameters, J. Geophys. Res, 86, 7639–7648, 1981.

Ridley, A. J., Lu, G., Clauer, C. R., and Papitashvili, V. O.: A statistical study of the ionsopheric convection response to changing interplanetary magnetic field conditions using the assimilative mapping of ionospheric electrodynamics technique, J. Geophys. Res., 103, 4023–4039, 1998.

Ruohoniemi, J. M., Greenwald, R. A., de la Beaujardière, O., and Lester, M.: The response of the high-latitude dayside ionosphere to a sudden southward IMF turning, Ann. Geophysicae, 11, 544–555, 1993.

Ruohoniemi, J. M. and Greenwald, R. A.: Statistical patterns of high-latitude convection obtained from Goose Bay HF radar observations, J. Geophys. Res., 101, 21 743–21 763, 1996.

Ruohoniemi, J. M. and Baker, K. B.: Large-scale imaging of high-latitude convection with Super Dual Auroral Radar Network HF radar observations, J. Geophys. Res., 103, 20 797–20 811, 1998.

Russell, C. T.: The configuration of the magnetosphere, in: Critical Problems of Magnetospheric Physics, (Ed) Dyer, R., Nat. Acad. of Sci., Washington, D.C., 1–16, 1972.

Sandholt, P. E., Farrugia, C. J., Moen, J., and Cowley, S. W. H.: Dayside auroral configurations: responses to southward and northward rotations of the interplanetary magnetic field, J. Geophys. Res., 103, 20 279–20 295, 1998a.

Sandholt, P. E., Farrugia, C. J., Moen, J., Noraberg, Ø., Lybekk, B., Sten, T., and Hansen, T.: A classification of dayside auroral forms and activities as a function of IMF orientation, J. Geophys. Res., 103, 23 325–23 345, 1998b.

Sandholt, P. E., Farrugia, C. J., Cowley, S. W. H., Lester, M., Moen, J., Lybekk, B., and Trondsen, E.: Excitation and decay of magnetospheric lobe cell convection and its associated aurora, Geophys. Res. Lett., 26, 3597–3600, 1999.

Sandholt, P. E., Farrugia, C. J., Cowley, S. W. H., Lester, M., Denig, W. F., Cerisier, J.-C., Milan, S. E., Moen, J., Trondsen, E., and Lybekk, B.: Dynamic cusp aurora and associated pulsed reverse convection during northward interplanetary magnetic field, J. Geophys. Res., 105, 12 869–12 894, 2000.

Sandholt, P. E., Farrugia, C. J., Cowley, S. W. H., and Lester, M.: Dayside auroral bifurcation sequence during B_y-dominated interplanetary magnetic field: Relationship with merging and lobe convection cells, J. Geophys. Res., 106, 15 429–15 444, 2001.

Senior, C., Cerisier, J.-C., Rich, F., Lester, M., and Parks, G. K.: Strong sunward propagating flow bursts in the night sector during quiet solar wind conditions: SuperDARN and satellite observations, Ann. Geophysicae, 20, 771–786, 2002.

Sergeev, V. A., Liou, K., Meng, C.-I., Newell, P. T., Brittnacher, M., Parks, G., and Reeves, G. D.: Development of auroral streamers in association with localized impulsive injections to the inner magnetotail, Geophys. Res. Lett., 26, 417–420, 1999.

Siscoe, G. L. and Huang, T. S.: Polar cap inflation and deflation, J. Geophys. Res., 90, 543–547, 1985.

Smith, C. W., Acuña, M. H., Burlaga, L. F., L'Heureux, J., Ness, N. F., and Scheifele, J.: The ACE Magnetic Field Experiment, Space Sci. Rev., 86, 613–622, 1999.

Stone, E. C., Frandsen, A. M., Mewaldt, R. A., Christian, E. R., Margolies, D., Ormes, J. F., and Snow, F.: The Advanced Composition Explorer, Space Sci. Rev., 86, 1–22, 1998.

Sutcliffe, P. R.: Observations of Pi2 pulsations in a near ground state magnetosphere, Geophys. Res. Lett., 25, 4067–4070, 1998.

Tsyganenko, N. A.: A magnetospheric magnetic field model with a warped tail current sheet, Planet. Space Sci., 37, 5–20, 1989.

Walker, A. D. M., Pinnock, M., Baker, K. B., Dudeney, J. R., and Rash, J. P. S.: Strong flow bursts in the nightside ionosphere during extremely quiet solar wind conditions, Geophys. Res. Lett., 25, 881–884, 1998.

Walker, A. D. M., Baker, K. B., Pinnock, M., Dudeney, J. R., and Rash, J. P. S.: Radar observations of magnetospheric activity during extremely quiet solar wind conditions, J. Geophys. Res., 10.129/2001JA000063, 2002.

Weimer, D. R.: Models of the high-latitude electric potentials derived with a least error fit of spherical harmonic coefficients, J. Geophys. Res., 100, 19 595–19 607, 1995.

Weimer, D. R.: Substorm influence on the ionospheric electric potentials and currents, J. Geophys. Res., 104, 185–197, 1999.

Yeoman, T. K., Milling, D. K., and Orr, D.: Pi2 pulsation polarisation patterns on the U.K. Sub-auroral Magnetometer Network (SAMNET), Planet Space Sci., 38, 589–602, 1990.